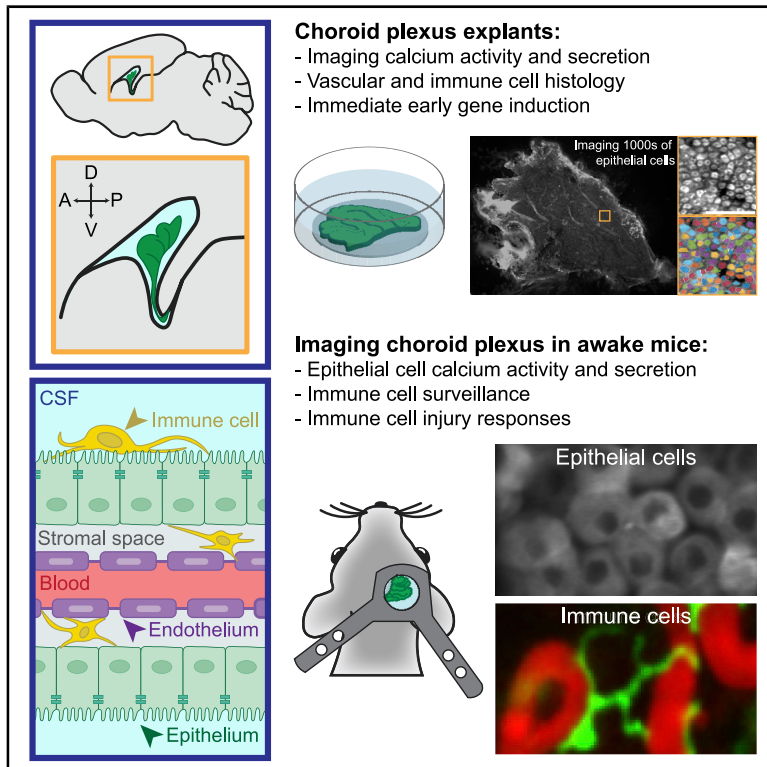


Neuron

Tracking Calcium Dynamics and Immune Surveillance at the Choroid Plexus Blood-Cerebrospinal Fluid Interface

Graphical Abstract



Authors

Frederick B. Shipley, Neil Dani, Huixin Xu, ..., Christopher I. Moore, Mark L. Andermann, Maria K. Lehtinen

Correspondence

manderma@bidmc.harvard.edu (M.L.A.), maria.lehtinen@childrens.harvard.edu (M.K.L.)

In Brief

The choroid plexus is a vital brain barrier and source of cerebrospinal fluid. Using two-photon imaging of choroid plexus epithelium in live explants and in awake mice, Shipley et al. establish a platform for investigating subcellular calcium activity and secretion in epithelial cells and diverse surveillance behaviors in immune cells.

Highlights

- Two-photon imaging of choroid plexus epithelium in live explants and in awake mice
- Spontaneous subcellular calcium events in epithelial cells in awake mice
- Serotonin boosts epithelial calcium activity and multiple forms of secretion
- Distinct surveillance and defensive behaviors in stromal and epiplexus immune cells



NeuroResource

Tracking Calcium Dynamics and Immune Surveillance at the Choroid Plexus Blood-Cerebrospinal Fluid Interface

Frederick B. Shipley,^{1,2,10} Neil Dani,^{1,10} Huixin Xu,¹ Christopher Deister,³ Jin Cui,¹ Joshua P. Head,¹ Cameron Sadegh,^{1,4} Ryann M. Fame,¹ Morgan L. Shannon,¹ Vanessa I. Flores,⁵ Thomas Kishkovich,³ Emily Jang,³ Eric M. Klein,³ Glenn J. Goldey,⁵ Kangmin He,^{6,9} Yong Zhang,⁷ Michael J. Holtzman,⁷ Tomas Kirchhausen,⁶ Claire Wyart,⁸ Christopher I. Moore,³ Mark L. Andermann,^{2,5,11,*} and Maria K. Lehtinen^{1,2,11,12,*}

¹Department of Pathology, Boston Children's Hospital, Boston, MA 02115, USA

²Graduate Program in Biophysics, Harvard University, Cambridge, MA 02138, USA

³Carney Institute for Brain Science, Brown University, Providence, RI 02912, USA

⁴Department of Neurosurgery, Massachusetts General Hospital, Harvard Medical School, Boston, MA 02114, USA

⁵Division of Endocrinology, Diabetes, and Metabolism, Department of Medicine, Beth Israel Deaconess Medical Center, Boston, MA 02115, USA

⁶Department of Cell Biology and Department of Pediatrics, Harvard Medical School, Program in Cellular and Molecular Medicine, Boston Children's Hospital, Boston, MA 02115, USA

⁷Pulmonary and Critical Care Medicine, Department of Medicine, Washington University, St. Louis, MO 63110, USA

⁸Institut du Cerveau et de la Moelle Épineuse (ICM), Sorbonne Université, Inserm U1127, CNRS UMR 7225, 75013 Paris, France

⁹Present address: National Laboratory of Biomacromolecules, Institute of Biophysics, Chinese Academy of Sciences, Beijing 100101, China

¹⁰These authors contributed equally

¹¹Senior author

¹²Lead Contact

*Correspondence: manderma@bidmc.harvard.edu (M.L.A.), maria.lehtinen@childrens.harvard.edu (M.K.L.)

<https://doi.org/10.1016/j.neuron.2020.08.024>

SUMMARY

The choroid plexus (ChP) epithelium is a source of secreted signaling factors in cerebrospinal fluid (CSF) and a key barrier between blood and brain. Here, we develop imaging tools to interrogate these functions in adult lateral ventricle ChP in whole-mount explants and in awake mice. By imaging epithelial cells in intact ChP explants, we observed calcium activity and secretory events that increased in frequency following delivery of serotonergic agonists. Using chronic two-photon imaging in awake mice, we observed spontaneous sub-cellular calcium events as well as strong agonist-evoked calcium activation and cytoplasmic secretion into CSF. Three-dimensional imaging of motility and mobility of multiple types of ChP immune cells at baseline and following immune challenge or focal injury revealed a range of surveillance and defensive behaviors. Together, these tools should help illuminate the diverse functions of this understudied body-brain interface.

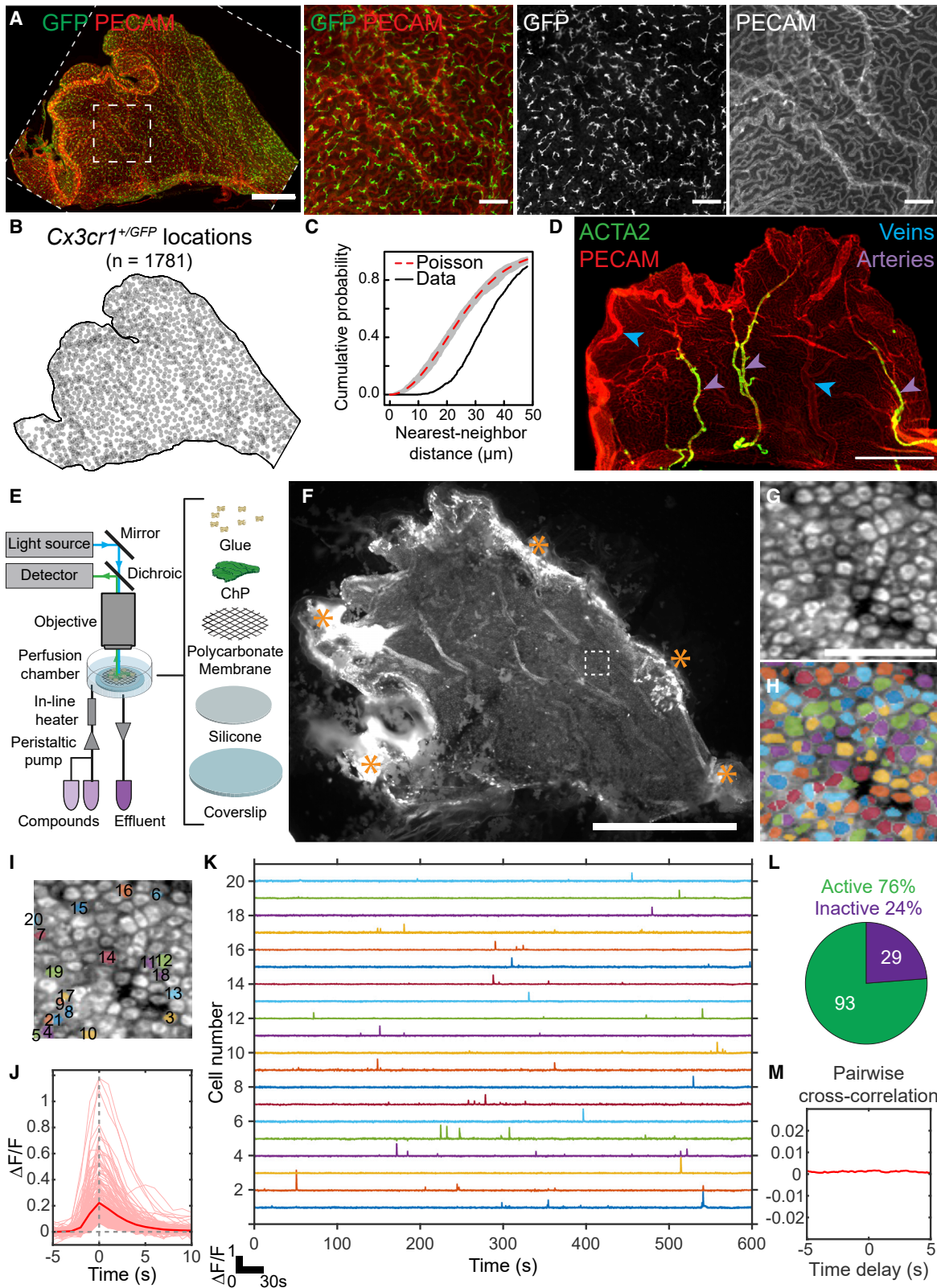
INTRODUCTION

The choroid plexus (ChP) is a distinct, vital organ that extends into each ventricle in the brain. It is composed predominantly of epithelial cells that envelop a network of stromal cell types, including immune, mesenchymal, and vascular cells (Dani et al., 2019). The epithelial cells provide a source of cerebrospinal fluid (CSF) (Damkier et al., 2013) and associated growth-promoting factors for neural stem cells (Lehtinen et al., 2011; Fame and Lehtinen, 2020; Silva-Vargas et al., 2016). They also form a blood-CSF barrier that gates passage of nutrients, toxins, and immune cells from body to brain (Gherzi-Egea et al., 2018; Reboldi et al., 2009; Schwartz and Baruch, 2014; Shechter et al., 2013) and may regulate CSF composition via clearance of toxins and waste (Crossgrove et al., 2005). Thus, the sensing, secretory, and transcytotic functions of the

ChP suggest diverse roles in regulating brain function. These roles may be disrupted in neurologic conditions ranging from hydrocephalus (Karimy et al., 2017) to Alzheimer's disease (Balusu et al., 2016a; Marques et al., 2013). Furthermore, the ChP is an attractive target for enhancing drug delivery to the brain (Gonzalez et al., 2011; Haddad et al., 2013; Hudry and Vandenberghe, 2019).

Despite the importance of the ChP-CSF system, little is known about the behavior of mammalian ChP cell types *in vivo*. *In vitro* approaches exist for culturing ChP cell lines (Zheng and Zhao, 2002), dissociated ChP cells (Zheng et al., 1998), ChP epithelial cell sheets in transwell models (Strazielle and Gherzi-Egea, 1999), and ChP organoids (Pellegrini et al., 2020; Watanabe et al., 2012). Isolated ChP explants have also been used for analyzing secretion into conditioned medium (Gudeman et al., 1987, 1989; Lun et al., 2015a; Silva-Vargas et al., 2016) or for fixation and





(legend on next page)

immunostaining (Dani et al., 2019; Lun et al., 2015a). Anatomical studies using light microscopy and electron microscopy (EM) have provided clues as to the cellular architecture of the ChP (e.g., Netsky and Shuangshoti, 1975). However, a major obstacle to progress in understanding the roles of ChP cells has been the lack of available tools for stable visualization and manipulation of specific ChP cell types in intact tissue *in vitro* and *in vivo* in a fluid environment deep within the brain.

Here, we adapted a suite of modern neuroscience tools to target the lateral ventricle (LV) ChP, providing optical access to this unexplored tissue in mice. We developed methods for volumetric two-photon imaging and non-rigid alignment of the ChP in acute explant preparations, as well as in awake mice across hours, days, and weeks. Dynamic cellular functions of other epithelia (e.g., in retina, lung, and salivary gland) are typically associated with changes in intracellular calcium (Ambudkar, 2016; Balaji et al., 2017; Concepcion and Feske, 2017; Narciso et al., 2017; Samanta and Parekh, 2016). For example, calcium signaling in salivary gland is important for on-demand secretion (Ambudkar, 2018, 2016). We found that ChP epithelial cells exhibited spontaneous subcellular calcium activity *in vitro* and *in vivo*. Serotonergic agonists evoked distributed increases in calcium activity, as well as secretory events measured using a sensor of exocytosis. We then visualized the motility and mobility of ChP immune cells in relation to ChP vasculature in awake mice at baseline and in response to peripheral immune stimulation and to laser-induced, focal ChP injury. Together, these methods provide a novel imaging platform for a wide range of studies imaging multiple genetically accessible ChP cell types in intact tissue at unprecedented spatial and temporal resolution.

RESULTS

Imaging ChP Explants

We first optimized adult LV ChP explant preparations (Dani et al., 2019; Lun et al., 2015a) to enable histological analyses (Figures 1A–1D) and stable live-cell imaging (Figures 1E, 1F, and S1A).

Epithelial cells constitute the majority of adult ChP cells (Dani et al., 2019). In addition, the ChP contains immune cells (labeled by $Cx_3cr_1^{+/GFP}$; Jung et al., 2000) consisting mostly of monocytes/macrophages but also including a smaller number of mast cells and dendritic cells (Dani et al., 2019; Van Hove et al., 2019). These immune cells evenly tiled the entire tissue under baseline conditions (Figures 1A–1C). The ChP could be divided into stereotyped zones defined by arterial and venous landmarks (Figures 1D, S1B, and S1C) (Dani et al., 2019). This vascular pattern strongly resembles that observed for human ChP (Hudson, 1960). As such, it provides an anatomical roadmap that allows specific subregions of the LV ChP to be identified and analyzed across mice within the same study, across studies from different labs, and across species.

ChP explants were stabilized for acute *in vitro* imaging (Figure 1E). To visualize calcium activity in epithelial cells, we gently dissected and stabilized the entire LV ChP from one hemisphere. We expressed the calcium reporter GCaMP6f (using *Ai95D* mice; Madisen et al., 2015) in ChP epithelial cells (using *FoxJ1-Cre* mice that selectively target this cell population) (Figure 1F) (Lun et al., 2015a; Zhang et al., 2007). Using epifluorescence imaging, we could visualize spontaneous calcium activity across thousands of epithelial cells simultaneously (Figure 1F; Video S1). We focused on a subregion and performed activity-based cell segregation (STAR Methods), resulting in time courses of spontaneous activity in individual epithelial cells (Figures 1F–1K; Video S1). Most epithelial cells showed large, transient elevations in calcium activity lasting several seconds (Figures 1K and 1L). Such events were not synchronized across cells (Figure 1M). These findings suggest baseline regulation of calcium levels and calcium-dependent signal transduction in ChP epithelial cells.

Activation of Serotonin Receptors Stimulates Secretion via VAMP3-Mediated Exocytosis

Elevated calcium regulates many cellular processes, including gene transcription and secretion in other body epithelia, such as the salivary gland (Ambudkar, 2016). One factor previously

Figure 1. Isolation, Immunostaining, and Calcium Imaging of Lateral Ventricle ChP Explants

- (A) Left: large leaf of LV ChP from a $Cx_3cr_1^{+/GFP}$ mouse immunostained with anti-GFP (green, immune cells) and PECAM (red, vasculature). Scale bar, 500 μ m. Right: zoom-in of small dashed box. Scale bar, 100 μ m. $Cx_3cr_1^{+/GFP}$ cells tile the ChP (confirmed in eight other mice).
- (B) Positions of 1,781 $Cx_3cr_1^{+/GFP}$ cells from (A).
- (C) Cumulative distribution of nearest-neighbor distances of each $Cx_3cr_1^{+/GFP}$ cell. Immune cells showed regular spacing (~ 30 μ m) relative to random Poisson spacing (red trace; gray envelope, 1% acceptance interval).
- (D) PECAM (red) and ACTA2 (green) immunostains demarcate stereotyped LV ChP regions (confirmed in three other mice). Purple arrowheads, arteries. Blue arrowheads, veins. Scale bar, 500 μ m.
- (E) Light path and setup for imaging LV ChP.
- (F) Epifluorescence image containing a *FoxJ1-Cre::Ai95D* LV ChP explant expressing GCaMP6f in multiciliated ChP epithelial cells. Cells near stabilizing glue attachments at explant borders (asterisks) showed elevated GCaMP6f fluorescence (indicating unhealthy cells) and were excluded from subsequent analyses. Scale bar, 1 mm.
- (G) Zoom-in of 122 epithelial cells (dashed box in F). Scale bar, 50 μ m.
- (H) Cell masks (see STAR Methods).
- (I) Twenty labeled cells corresponding to traces in (K).
- (J) Pink, traces surrounding each calcium transient with a fractional change in fluorescence, $\Delta F/F > 5\sigma$ (235 events across 122 cells from H). Red, mean calcium transient across traces.
- (K) Five-minute time courses from cells in (I).
- (L) Seventy-six percent of cells (93 of 122) in (H) exhibited calcium events.
- (M) Average of all cross-correlations between binarized event time courses of all pairs of cells from (H) (computed at delays from -5 to $+5$ s), demonstrating that spontaneous events were uncorrelated across cells. We observed qualitatively similar results as in (G)–(M) in 25 other mice (not shown). See also Figure S1; Video S1.

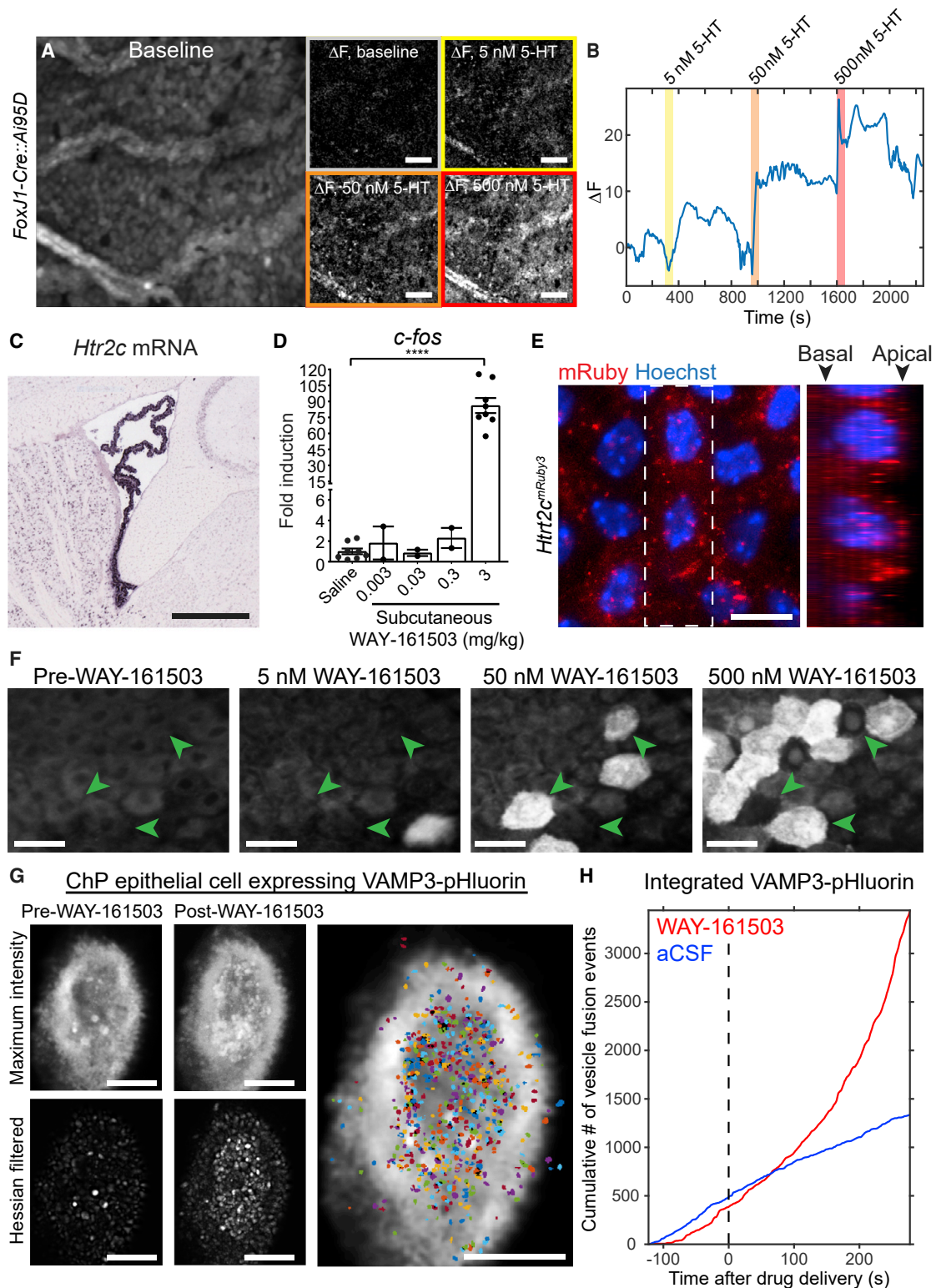


Figure 2. Evoked Calcium Activity and Exocrine Secretion in ChP Epithelial Cells

(A) Epifluorescence calcium imaging of ChP epithelial cells from *FoxJ1-Cre::Ai95D* LV ChP explant. Mean baseline fluorescence (left) and changes in fluorescence from baseline in response to 0, 5, 50, and 500 nM 5-HT. Scale bar, 100 μ m.

(legend continued on next page)

shown to elevate calcium levels in ChP cell lines in culture is serotonin (5-HT [5-hydroxytryptamine]) (Esterle and Sanders-Bush, 1992; Sanders-Bush and Breeding, 1990). Metabolites of the 5-HT signaling pathway are present in the CSF (Toda et al., 2013). CSF-5-HT can originate from multiple sources, including direct release by dorsal raphe nucleus serotonergic neurons that course along the ventricles and in close proximity to the ChP (Narboux-Nême et al., 2008; Okaty et al., 2020; Tong et al., 2014), and via peripheral circulation, originating, for example, from 5-HT secretion in the gut (Stasi et al., 2019) or platelets (Cloutier et al., 2012). We found that 5-HT (Audhya et al., 2012; Toda et al., 2013) triggered coordinated waves of calcium activity that recruited increasing numbers of ChP epithelial cells across the explant with higher concentrations of 5-HT (Figures 2A, 2B, and S2E; Video S2).

The 5-HT_{2C} serotonin receptor (Figure 2C) (Lein et al., 2007), a Gq/G₁₁-coupled G protein-coupled receptor (GPCR), is the most highly expressed GPCR in ChP epithelial cells (Lun et al., 2015a). We found that subcutaneous (s.c.) injection of WAY-161503, a selective agonist of 5-HT_{2C} (Rosenzweig-Lipson et al., 2006), drove robust immediate-early gene expression in ChP (Figures 2D, S2A, and S2B). Antibodies available for this receptor have typically shown low signal quality. Thus, we used genome editing to generate a *Htr2c*^{mRuby3} mouse line in which the fluorescent protein mRuby3 was inserted at the C-terminus of 5-HT_{2C} (Figures S2C and S2D). 5-HT_{2C}-mRuby3 was functional in these mice, as subcutaneous injection of WAY-161503 in *Htr2c*^{mRuby3} mice induced *c-fos* expression similar to that observed in wild-type mice (Figure 2D; mean ± SEM fold increase in *c-fos* mRNA expression in *Htr2c*^{mRuby3} mice receiving WAY-161503 [3 mg/kg] versus vehicle 80.6 ± 17.3, n = 4 heterozygous male mice; *Htr2c* expressed from X chromosome). Fluorescence of the mRuby3 tag revealed receptor localization throughout ChP epithelial cells, including at the apical and basal membranes (Figure 2E). This localization is consistent with the prediction that ChP epithelial cells can sense both central and peripheral sources of 5-HT (Figure S1C). Accordingly, using higher magnification two-photon calcium imaging, we obtained similar patterns of activation of an increasing number of cells with increasing concentrations of the 5-HT_{2C} agonist WAY-161503 (Figures 2F and S2E; Video S3).

Application of 5-HT to dissociated ChP cells in culture can increase the transfer of water and protein secretion (Conn and Sanders-Bush, 1986; Esterle and Sanders-Bush, 1992; Watson et al., 1995). Our expression analyses confirmed that the secre-

tory machinery commonly required for calcium-dependent gene induction, protein secretion, vesicle trafficking/release machinery, and/or homologs of proteins from other epithelia are expressed in ChP epithelial cells (e.g., *Vamp3*, *Snap23*, *Stx12*, *Stxbp4*), implicating vesicular exocytosis as a mechanism of protein secretion (Figures S2F–S2J) (Dani et al., 2019; Lun et al., 2015a). In EM images of ChP epithelial cells, a high density of vesicles was observed near the apical membrane (Figure S2I, black arrows). VAMP3 showed the highest gene expression among vesicle proteins in the ChP (Figure S2G; RNA sequencing [RNA-seq] data from Lun et al., 2015a), and VAMP3 protein expression was confirmed by immunoblotting and immunostaining (Figures S2H and S2J). These data led us to investigate activity-dependent and VAMP3-mediated ChP exocytosis. Specifically, we used AAV-VAMP3-pHluorin (Urbina et al., 2018), a pH-sensitive variant of GFP, to visualize individual secretory events. pHluorin fluoresces upon plasma membrane fusion, when the lower pH (~5.6) inside intact exocytic vesicles changes to a pH of 7.4 upon exposure to the extracellular environment. The fluorescence signal disappears following endocytosis and re-acidification of the vesicles (Sankaranarayanan et al., 2000).

We first expressed VAMP3-pHluorin in the Z310 ChP epithelial cell line (Zheng and Zhao, 2002). Using total internal reflection fluorescence (TIRF) microscopy, a method with high signal-to-noise ratio, fast frame rate (2 frames/s), and narrow fluorescence excitation and emission ranges, we could capture numerous spontaneous vesicle fusion events (Figure S2K; Video S4). To evaluate ChP secretion in a more naturalistic setting, we transduced ChP *in vivo* with AAV-VAMP3-pHluorin, dissected ChP explants, and investigated vesicle fusion events *in vitro*. Because of the elaborate apical structure of ChP epithelial cells, including multiple microvilli and cilia (Figure S2I), these cells were not amenable to TIRF microscopy (axial resolution < 100 nm) without compressing the cells against a coverglass, a procedure that could compromise cellular integrity or induce cellular responses to mechanical distortion. Instead, we used Airyscan confocal microscopy (ZEISS LSM880) that afforded comparable signal-to-noise ratio and frame rates (1.59 frames/s). We observed spontaneous VAMP3-mediated exocytosis in individual epithelial cells in whole ChP explants (Video S5). To monitor localized secretion events, we first performed spatial filtering of each image (Figure 2G). We then defined regions with co-active pixels and extracted fluorescence time courses (Figures 2G, 2H, and S2L). Strikingly, 5-HT_{2C} activation by WAY-161503 (delivered at levels similar to those that drove calcium activity in Figure 2F)

(B) Time course of changes from baseline, averaged across the explant. Responses to at least one dose of 5-HT were observed in 18 of 19 mice and to all three doses in 10 of 19 mice (not shown).

(C) *Htr2c* expression in LV ChP (from Allen Brain Atlas; Lein et al., 2007). Scale bar, 500 μm.

(D) *c-fos* induction following injection of 5-HT_{2C} agonist WAY-161503 (****p < 0.0001, t test, saline versus 3 mg/kg s.c.; left to right, n = 8, 2, 2, 2 and 8).

(E) *Htr2c*^{mRuby3} LV ChP labels 5-HT_{2C} receptors in epithelial cells. Axial (left) and side-on (right; from dashed box at left) maximum projections show preferential apical (apposed to the CSF) versus basal (closer to vessels) localization. Scale bar, 10 μm.

(F) Two-photon imaging of *FoxJ1-Cre::Ai95D* explants. Higher concentrations of WAY-161503 activated more cells (green arrowheads), and cells activated at lower concentrations are not reactivated later. Responses were observed in 7 of 7 mice and to each dose in 5 of 7 mice (not shown). Scale bar, 10 μm.

(G) Confocal imaging of vesicle release from an example LV ChP epithelial cell following viral expression of VAMP3-pHluorin. Top left: maximum-intensity projection across baseline period shows fluorescent vesicle release (white punctae). Bottom left: similar projection following Hessian-based filtering. Middle panels: same as left but following application of WAY-161503 (500 nM). Right: vesicle release event masks segmented from the filtered movie. Scale bar, 5 μm.

(H) Cumulative number of VAMP3-pHluorin vesicle release events following application of WAY-161503 (red) or aCSF (blue).

See also Figure S2; Videos S2, S3, S4, and S5.

drove an increase in the rate of VAMP3-mediated exocytosis (Figures 2H and S2L; Video S5). Our data using live imaging at subcellular resolution demonstrate that 5-HT stimulates ChP exocytosis via activation of 5-HT_{2C}. More generally, our findings validate a platform for fluorescence imaging in ChP explants, enabling high-resolution studies of calcium activation, secretion, and other processes.

In Vivo Imaging of ChP in Awake Mice

Virtually nothing is known about the activity of ChP cell types *in vivo*. We developed a deep-brain cannula implantation strategy that enables acute and longitudinal imaging of the ChP over weeks and months in awake mice. A cannula and glass window were surgically implanted above the LV (Figures 3A–3D), similar to our recent approach for imaging in visual thalamus (Liang et al., 2018). At 2–3 weeks post-surgery, windows were typically translucent, allowing bright-field imaging of ChP (Figure 3E).

Similar to brain surgery in the clinical setting, insertion of the imaging cannula is an invasive procedure. We performed additional control experiments to determine the extent of the injury response and to verify the health of the preparation several weeks following surgery, at the time of imaging. As anticipated, GFAP-positive astrocytes and *Cx₃cr₁*-positive immune cells were enriched in cerebral cortical tissue adjacent to the cannula (Figures S3A–S3G). The density of glial cells (GFAP positive) and immune cells (*Cx₃cr₁*-positive) dropped to baseline levels by ~100 μ m from the edge of the cannula (Figures S3A–S3G). The ventricular lining of the LV below and lateral to the implant did not show accumulation of GFAP- or *Cx₃cr₁*-positive cells and retained characteristic S100 β -positive ependymal cells (Figure S3B). Importantly, immune cells from the ChP tissue located below the implant exhibited a ramified, non-activated morphology with extended processes and a level of tiling of the ChP that was indistinguishable from observations in contralateral ChP and in ChP from control mice that did not undergo surgery (see Figures 1A–1C, S3H, and S3I). Elevated CSF cytokine levels that were evident in some mice 1 day following surgery also returned to undetectably low levels in all mice by 3 weeks post-surgery (Figure S3J). These data demonstrate that at the time imaging began several weeks post-surgery, our imaging preparation did not show signs of persistent inflammation.

Epifluorescence images of LV ChP from transgenic mice expressing GCaMP6f in ChP epithelial cells (*FoxJ1-Cre::Ai95D*; Figure 3F; Video S6) demonstrated consistently high image quality across mice. Notably, anatomical features of the ChP were stable upon repeated imaging across weeks and months, with no evidence of substantial remodeling of vasculature across imaging sessions beginning several weeks following surgery (Figure 3G). Although the location of the ChP in the LV showed moderate mouse-to-mouse variability following surgery (Figure 3F), identification of arterial and venous landmarks allowed longitudinal imaging of a similar anatomical region of the ChP across mice and within the same mouse across sessions (Figures 3 and S1B).

To maximize spatial resolution and minimize bleaching during cellular imaging, we performed two-photon imaging using a long-working distance, high-numerical aperture objective

coupled to the imaging window (see STAR Methods). We targeted local regions of interest within previously acquired epifluorescence images (Figures 4A–4C). In contrast to other brain tissues that can be largely pressurized and stabilized for two-photon imaging (Goldey et al., 2014; Liang et al., 2018), the ChP is only anchored at one edge near the base of the LV and is otherwise suspended in CSF. Therefore, the ChP often exhibited large and non-rigid motion in three dimensions during changes in behavior such as locomotion or adjustment of body posture (Video S6). As described below, we used different imaging strategies and custom registration algorithms to overcome these technical challenges.

First, video-rate two-photon imaging of a single plane allowed precise and high-speed tracking of small numbers of cells following in-plane alignment, particularly during periods of minimal brain motion while the mouse was stationary. For these analyses, occasional large tissue movement could be stabilized or omitted from further analyses. Second, for longitudinal tracking across hours, for which larger non-rigid motion and drift of the tissue out of plane were often evident, we instead used a volumetric imaging strategy (0.25–0.5 volumes/s, 31–62 planes/volume, volume dimensions 170 \times 170 \times 350 or 355 \times 230 \times 100 μ m³; see STAR Methods). This approach was important for achieving stable cell tracking following non-rigid alignment in three dimensions (see Figure 5).

Imaging Calcium Activity and Apocrine Secretion in ChP Epithelial Cells *In Vivo*

We imaged ChP epithelial cell calcium activity using a transgenic mouse expressing GCaMP6f, which provided similar expression levels across cells and stable expression across days (Figures 4A–4C; see also Figure 1F). We first performed single-plane two-photon calcium imaging (Figure 4D). High-speed imaging (33–41 frames/s) revealed spontaneous subcellular calcium events lasting ~200 ms (Figure 4G; Videos S7 and S8). To quantify this observation, we manually outlined the borders and nuclei of individual cells (Figures 4D–4F). A typical subcellular event from one example cell is shown in Figure 4G. We segmented each cell into 12 radial sectors extending from the center of the nucleus (Figure 4E, bottom) and “unwrapped” the sectors to create a kymograph of averaged subcellular activity across frames (Figure 4H). A maximum-intensity projection across sectors revealed large subcellular events (Figure 4I) of a consistent duration and characteristic exponential decay (Figure 4J). The consistent dynamics and correlated changes across nearby pixels for this and other cells (Figure S4) further suggested that these events were not due to photon noise or brain motion. In contrast to maximum-intensity projections across sectors, median projections showed no significant fluctuations (Figures 4K, S4A, and S4B), consistent with the subcellular nature of these events.

Our earlier findings demonstrated that application of 5-HT_{2C} agonist WAY-161503 evoked robust calcium responses in ChP epithelial cells *in vitro* and induced immediate-early gene expression following peripheral injection *in vivo* (Figures 2D, 2F, S2A, S2B, and S2E; Video S3). Furthermore, signatures of apocrine secretion (Figures 4M and 4N; Video S9) have previously been reported to occur in ChP *ex vivo* (Agnew et al., 1980; Farkaš,

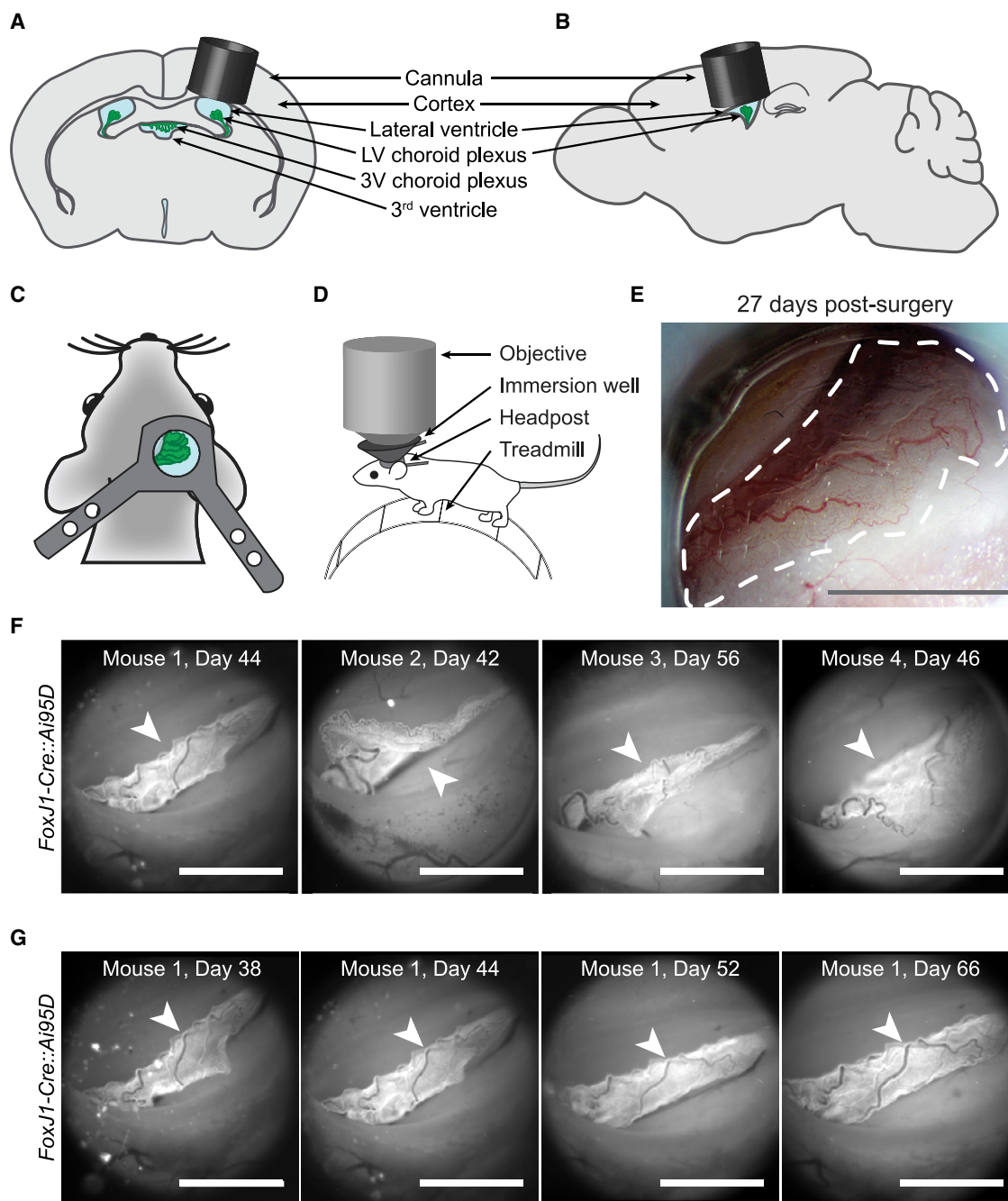


Figure 3. Imaging Lateral Ventricle ChP in Awake Mice

(A and B) Schematic of cannula (gray cylinder) with glass bottom, implanted above the LV ChP (green).

(C) Headpost placement.

(D) Head-fixed mouse on a trackball. An immersion well attached to the headpost allowed imaging using a high numerical aperture objective.

(E) Bright-field image of ChP through the cannula 27 days post-surgery. Dotted line outlines ChP. Scale bar, 1 mm.

(F) Epifluorescence images of ChP (arrowheads) from *FoxJ1-Cre::Ai95D* mice, 42–56 days after surgery. Scale bar, 1 mm.

(G) Tracking the same ChP (arrowheads) through a clear window across many days following surgery (similar results observed in nine other mice, not shown). Scale bar, 1 mm.

See also [Figure S3](#); [Video S6](#).

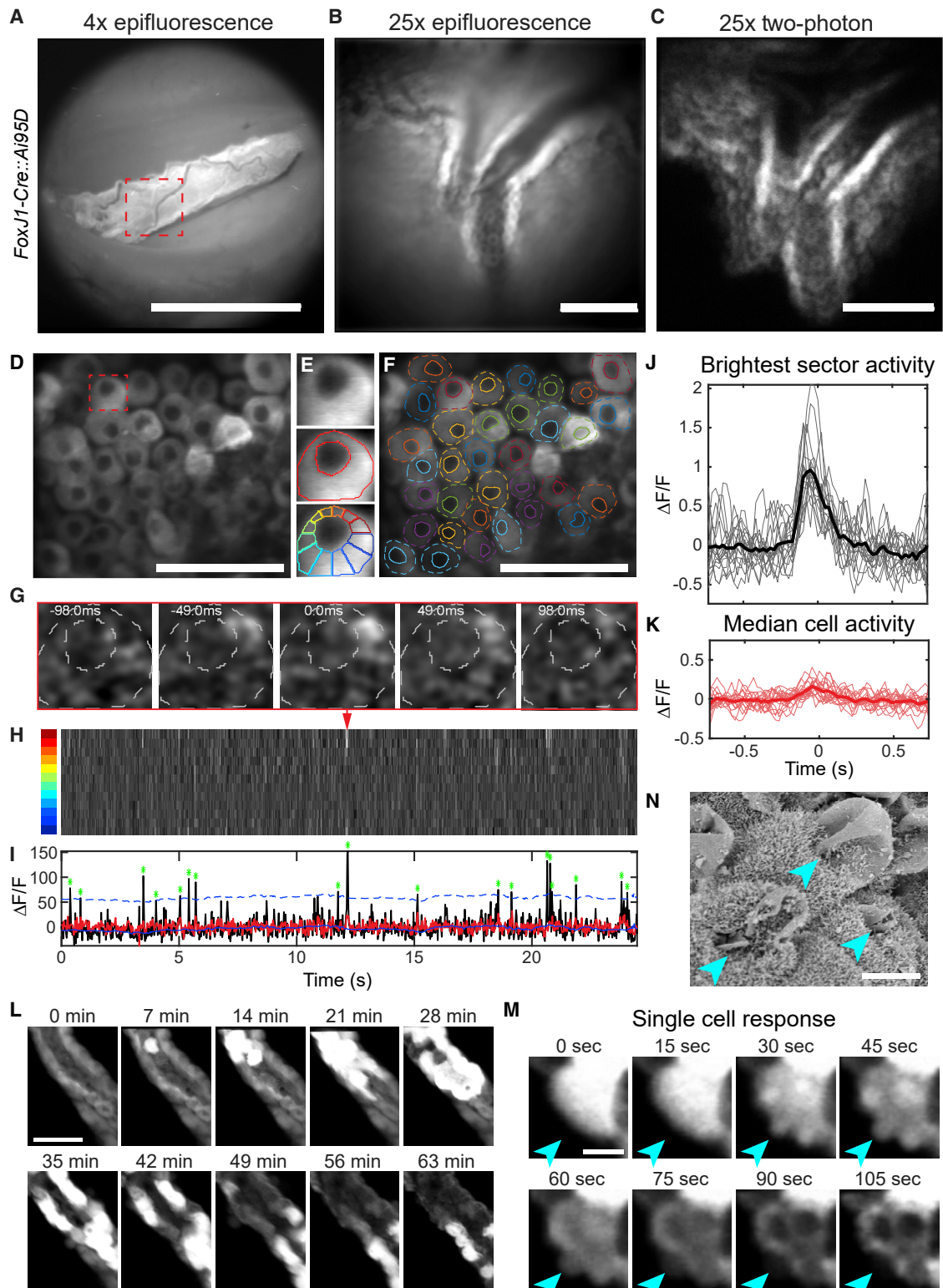


Figure 4. Two-Photon Calcium Imaging of Epithelial Cells in Awake Mice

(A) Epifluorescence image of GCaMP6f-expressing ChP epithelial cells (diagonal vascularized sheet; *FoxJ1-Cre::Ai95D* mouse). Scale bar, 1 mm. (B) Zoomed-in image (dashed red square in A). Scale bar, 100 μ m.

(legend continued on next page)

2015; Gudeman et al., 1989). We therefore sought to define the dynamics of ChP calcium activity and apocrine secretion upon WAY-161503 delivery *in vivo*. To obtain stable estimates of calcium transients across tens of minutes (see above), we used volumetric imaging (0.32 volumes/s, 93 planes/volume, 3.8 μm spacing between planes). Subcutaneous injection of WAY-161503 resulted in robust increases in calcium activity that progressed along the epithelium over tens of minutes (Figure 4L; Video S9). The large differences in timing of activation of various cells may relate to cell-to-cell differences in 5-HT_{2C} expression (Figure 2E), to slow changes in the concentration of WAY-161503, or to sequential sensing of signals released from activated neighboring cells. Cellular increases in calcium activity culminated in apocrine secretion, reflected by a release of cytoplasmic protrusions from the apical surface of the cell and cellular release of cytoplasmic contents directly into the CSF (Figures 4L–4N; Video S10). The basal portion of the cells including the nucleus remained intact. Taken together, these findings highlight novel *in vitro* and *in vivo* approaches to test and visualize calcium activity and distinct modes of exocrine signaling by ChP epithelial cells. Furthermore, these data establish a platform for testing how exogenous signals such as serotonin can stimulate calcium activation, gene transcription, and exocrine secretion.

ChP Immune Cells at Baseline and in Response to Local or Peripheral Stimulation

The ChP is not only important for secretion of water and proteins into the CSF but is also an essential barrier that protects the brain from harmful blood-borne factors (Gherssi-Egea et al., 2018; Saunders et al., 2018) and is implicated as a site of immune cell entry into the brain (Fame and Lehtinen, 2020; Gherssi-Egea et al., 2018; Reboldi et al., 2009; Schwartz and Baruch, 2014; Shechter et al., 2013). However, the *in vivo* functions of ChP immune cells in physiological or pathological conditions remain largely unexplored (Kierdorf et al., 2019). Thus, we investigated ChP immune cells under homeostatic, immune-challenged, and injury conditions.

We repeated the surgical approach described above in transgenic mice expressing GFP in *Cx₃cr₁*-positive immune cells (Jung et al., 2000). Following surgical recovery, we performed intraperitoneal (i.p.) injection of Texas red-conjugated dextrans

that rapidly filled the major vessels and fine capillary networks of the ChP. These large dextrans (70 kDa) did not immediately leak into the ChP stromal space. We then performed two-color imaging of ChP immune cells and vasculature (Figure 5A), focusing on regions of ChP that were oriented parallel to the imaging plane and thus amenable to time-lapse volumetric imaging across the thickness of the tissue (Video S11).

For tracking of fine immune cell processes across seconds, minutes, and hours in awake mice, it was critical to develop a procedure for accurate alignment of the three-dimensional (3D) imaging volumes (see Figure 5B and legend). It was useful to estimate shifts in ChP using the stable, bright red dextran signal and then apply these shifts to both the imaged vasculature (red) and immune cells (green). Given that the individual frames were acquired at 15.5 frames/s, there was minimal within-plane non-rigid motion. However, brain motion could result in X and Y shifts in successive imaging planes within a volume (Video S12). Thus, alignment of each Z plane to a reference plane within each volume was important (Figures 5C and 5D). We then performed rigid-body 3D alignment. Following these corrections, images of static objects (e.g., vasculature) could be effectively stabilized (Figures 5E and 5F). As a final step, we calculated the mean intensity across Z planes for each volume and ran a second translational alignment. Across all 20 sessions from 13 mice, estimated intra-volume and inter-volume shifts in X, Y, and Z could be quite large, reflecting ChP suspension in CSF (Figures 5G–5J).

We observed substantial exploratory movements of ChP immune cell bodies and/or distal processes. In each of 26 fields of view from 14 mice, we observed large numbers of GFP-positive immune cells. Some of the cells were located within the ChP stromal space, while others were located on the apical surface of the ChP, in contact with LV CSF (i.e., epileptus or Kolmer cells) (Figures 6A–6G). Epileptus cell bodies often exhibited substantial mobility. For example, the cell in Video S13 (top left) traveled 210 μm in 1 h. Some epileptus cell bodies moved at a constant rate, while others displayed saltatory movements (Figure 6D; Video S13). In contrast, the majority of GFP-positive immune cells located within the stromal space showed minimal cell body mobility. However, these cells possessed highly dynamic processes that extended and contracted (Figures 6E–6G; Video S13), similar to microglia in other brain areas (Hiero-Bujalance

(C) Maximum projection of two-photon imaging volume encompassing the ChP region in (B). Scale bar, 100 μm .

(D) Average of images at a single plane. Scale bar, 50 μm .

(E) Individual epithelial cell (red square in D), annotation of cell outline and nucleus, and division into 12 sectors.

(F) Annotation of all cell outlines and nuclei in (D).

(G) Time-lapse of a single subcellular calcium event.

(H) Kymograph of activity across all 12 sectors of cell in (E) and (G). Red arrowhead, event from (G).

(I) Time course of brightest-sector activity (black, maximum across sectors in H) and median activity (red). Asterisks, peaks of subcellular events exceeding 3 SDs (dashed blue line) above a running mean.

(J and K) Brightest-sector (J) and median-sector (K) activity surrounding peak ($t = 0$) of all events for cell in (E). Thicker lines, mean traces. Similar results were observed in three other mice (not shown).

(L) Images of cross-sections of two sheets of GCaMP6-expressing epithelial cells separated by stromal space, beginning 25 min after injection of WAY-161503 (3 mg/kg, s.c.; similar results observed in two other mice, not shown). Scale bar, 50 μm .

(M) Zoom-in of a single epithelial cell reveals release of subcellular plumes (arrowheads) of intracellular contents including GCaMP6f into CSF. The basal side of the epithelium remained intact, consistent with apocrine secretion. Scale bar, 10 μm . Similar events were observed in a second mouse (not shown). See also Figure S4; Videos S7, S8, S9, and S10.

(N) Scanning EM of ChP 15 min following WAY-161503 (3 mg/kg, s.c.) reveals apocrine blebs (arrowheads). Scale bar, 5 μm .

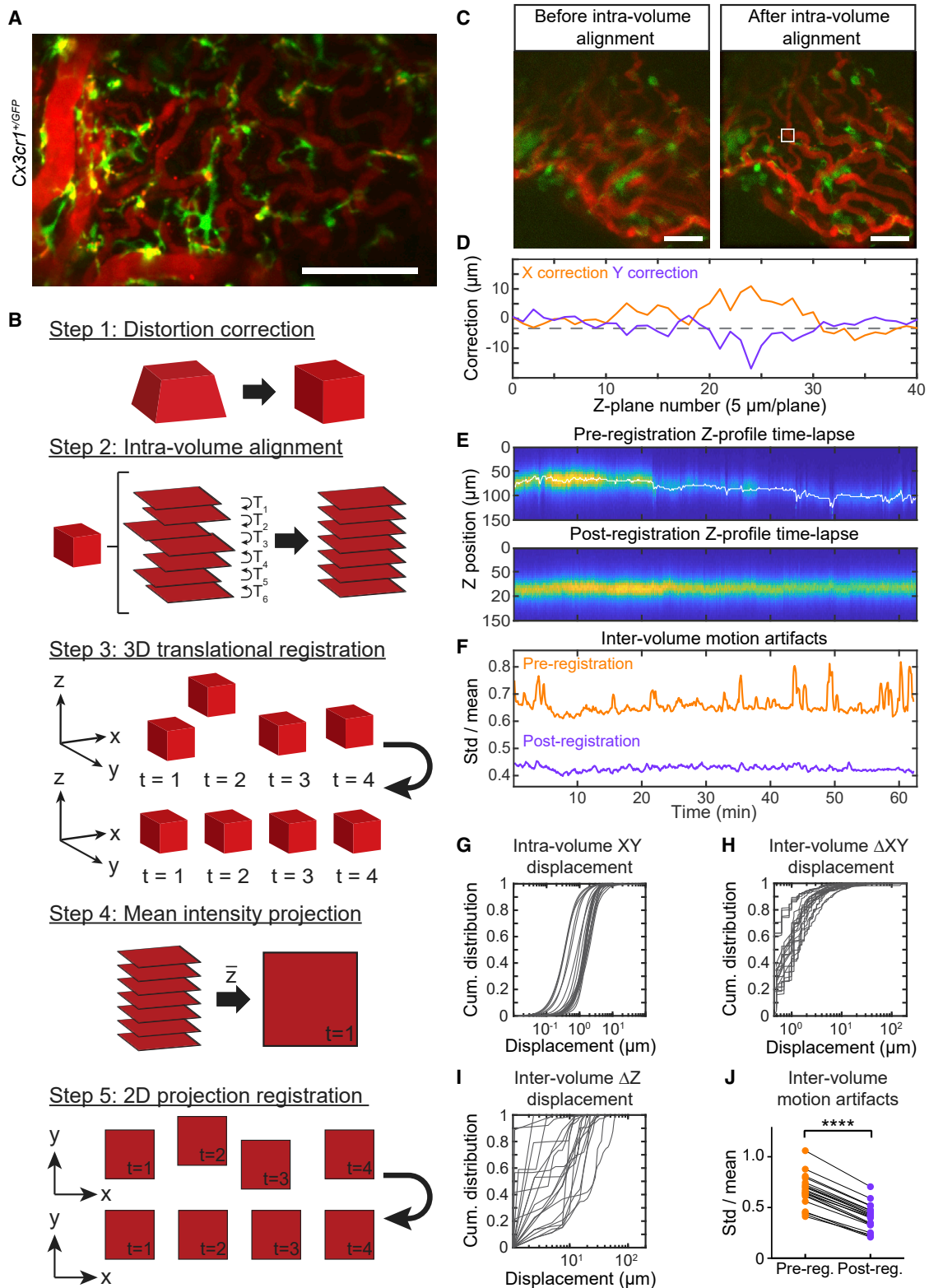


Figure 5. Three-Dimensional Imaging and Registration of ChP in Awake Mice

(A) Maximum projections across a time-averaged two-photon imaging volume of $Cx_3cr1^{+/GFP}$ immune cells (green) and Texas red dextran-labeled vasculature (red; i.p. injection). Projections from two mice are shown (similar results in 13 other mice, not shown). Scale bar, 100 μm .

(legend continued on next page)

et al., 2018). These processes appeared to serve a surveillance function, as they frequently contacted vessels within the stromal space and retracted upon contact with other processes from the same or neighboring immune cells (Figures 6E–6G; Video S13).

These surveillance-like behaviors were reminiscent of immune cells in other parts of the brain that play key roles in sensing environmental perturbations and protecting against injury (Hickman et al., 2018; Kierdorf et al., 2019; Li and Barres, 2018). Indeed, we found that immune cells in the ChP appear to partake in similar functions. First, we noted that the fluorescent dextrans used to label vasculature were cleared from circulation over several days. In these experiments, ChP immune cells in the stromal space, but not epiplexus cells, took up fluorescent dextrans 30 min following injection (Figures 6H and 6I; Videos S14 and S15), and dextran-labeled punctae could be observed even 26 days following injection (Figures S5A–S5C). These data demonstrate that ChP immune cells participate in uptake of foreign material from the peripheral circulation, consistent with the known housekeeping functions of immune cells in other parts of the body and brain.

The ChP contributes to blood-brain communication during peripheral inflammation (Balusu et al., 2016b), and the effects of immune challenges on the ChP have been implicated in several neurologic conditions. For example, genetic markers of immune function and inflammation are upregulated in ChP of schizophrenia patients (Kim et al., 2016). Thus, we next considered the effects of peripheral administration of the bacterial endotoxin lipopolysaccharide (LPS), which induces inflammatory responses in mouse ChP (Balusu et al., 2016b; Marques et al., 2009), on ChP immune cell morphology *ex vivo* and *in vivo*. As expected, LPS induced an inflammatory cytokine response in serum and CSF (Figures 7A and S6A). Using immunohistochemistry, we found that although peripheral LPS administration did not affect tiling of immune cells across the ChP (Figures 1A–1C, S3H, and S3I), it triggered a marked repositioning of GFP-positive immune cell bodies and processes to regions surrounding the vasculature within the ChP (Figures 7B, 7C, and S6B).

To define the morphological dynamics of individual immune cells in response to LPS, we performed *in vivo* two-photon imaging during peripheral delivery of LPS. Many GFP-positive ChP immune cell bodies and processes that were initially located distal to vessels prior to LPS moved toward and spread along nearby vessels within ~45–60 min of LPS delivery (Figure 7D; Video S16). Using a custom algorithm to segment vasculature and define periluminal regions (Figures 7E, 7F, and S6C; STAR Methods), we confirmed that immune cell fluorescence

increased in periluminal regions (Figure 7F). Not all *Cx₃cr₁*-expressing cells responded to LPS, consistent with the multiplicity of *Cx₃cr₁*-expressing ChP immune cell types that likely exhibit distinct responses to peripheral stimuli (Dani et al., 2019; Van Hove et al., 2019). This repositioning of ChP immune cells along the periluminal region may provide an extra layer of brain protection from harmful blood-borne signals during peripheral inflammation (Mottahedin et al., 2019).

In addition to the robust response of ChP immune cells following peripheral inflammation, we found that these cells often move toward sites of local injury. We induced a focal injury by high-power two-photon heating of a small area in the center of the field of view (89 × 57 μm²; Figure 7G). This triggered rapid recruitment of immune cells to the injury site from nearby regions of the ChP. Immune cells initiated movement immediately following the laser injury, transitioned to an apparently more activated state (retracted processes, larger cell bodies), and continued moving until they stabilized in an aggregate surrounding the injury site (Figure 7H; Video S17). Across three mice, most but not all immune cells moved toward the injury site (Figure 7I). The majority of the cells that did move toward the injury site were confirmed to be epiplexus cells (Video S18). Together, these findings reflect diverse contributions of different types of resident ChP immune cells to host defense.

DISCUSSION

The scarcity of experimental tools for selectively targeting, monitoring, and manipulating ChP cells has hindered progress in understanding this essential and distinct organ located deep within the brain. Despite its principal roles in producing CSF, forming a brain barrier, and secreting important health and growth-promoting factors for the brain (Fame and Lehtinen, 2020; Ghersi-Egea et al., 2018; Lun et al., 2015b; Saunders et al., 2018), remarkably little is known regarding the functions of its cellular networks. Here, we developed imaging and analysis approaches for monitoring and pharmacological manipulation of multiple ChP cell types in live explants and in awake mice. Using a combination of epifluorescence, confocal, and two-photon microscopy in ChP explants, we observed spontaneous calcium activity as well as spontaneous exocytotic fusion events in individual epithelial cells. Both of these processes were enhanced by application of agonists of the 5-HT_{2C} receptor, which is highly expressed in ChP epithelial cells. Epifluorescence and two-photon microscopy in awake mice revealed subcellular spontaneous calcium activity and 5-HT_{2C} agonist-evoked calcium activity and apocrine-type exocrine release.

(B) Registration algorithm (see STAR Methods). Step 1: correct for depth-dependent magnification due to tunable lens. Step 2: intra-volume alignment of each plane to its neighbor. Step 3: 3D translation of each volume to a local target. Steps 4 and 5: Z projection and X-Y alignment.

(C) Mean Z projection of a single volume before versus after step 2. Scale bar, 50 μm.

(D) Estimated X and Y corrections for each plane of volume in (C).

(E) Z-profile time lapse of vasculature before and after 3D registration. Columns, 600 volumes spanning ~63 min; rows, average fluorescence in the white box in (C) at each Z plane. White trace, estimated Z correction.

(F) Index of motion artifact (sliding estimate of SD/mean vasculature fluorescence across volumes; see STAR Methods). Registration reduced both large, transient motion artifacts (peaks in orange trace) and persistent, higher frequency motion (see J).

(G–I) Cumulative distributions of X and Y displacements of planes within each volume (G) and XY displacements (H) and Z displacements (I) across consecutive volumes. Data in (G)–(J) are from 20 sessions from 13 mice.

(J) Mean motion artifact (see F) per session, pre- versus post-registration. ****p < 0.0001, paired t test.

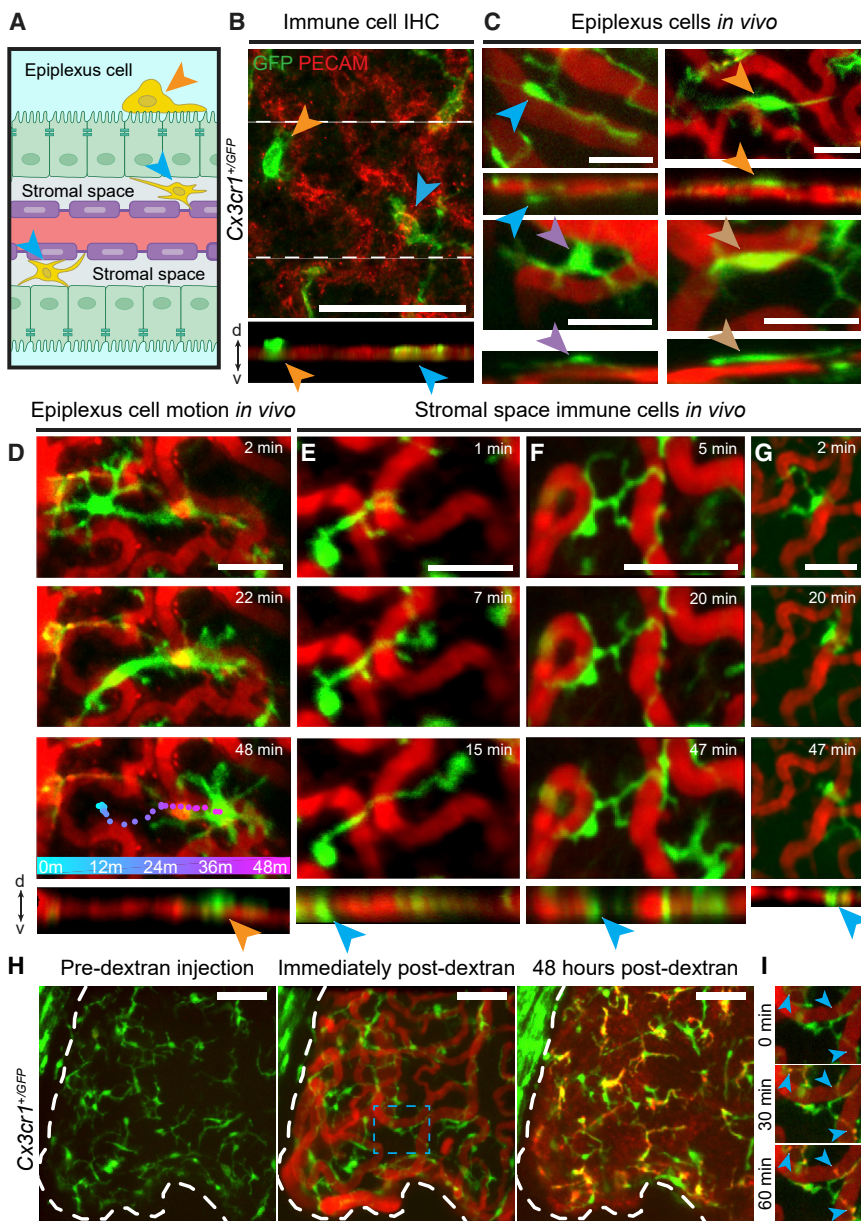


Figure 6. ChP Immune Cells Perform Local Surveillance and Housekeeping *In Vivo*

(A) Cross-section of ChP. Epilexus immune cells (orange arrowhead) are located on apical (CSF-sensing) surface of epithelium (green sheet). Stromal immune cells (blue arrowheads) are located in stromal space between vasculature (red with purple endothelial cells) and epithelium. (B) Top: axial mean projection of Cx₃Cr1^{+/GFP} cells in LV ChP explant *ex vivo*. Bottom: side-on view. Arrowheads indicate stromal (blue) and epilexus (orange) immune cells. Scale bar, 100 μm.

(C–G) Similar to (B) but from *in vivo* two-photon imaging (see also Videos S11 and S13). Scale bar, 25 μm. (C) Example epilexus cells from four mice. Side-on views (bottom) indicate locations outside vascular plane (likely outside the epithelium). (D) Example epilexus cell pausing, then traveling across the ChP surface (colored dots, cell location at 1 min intervals). (E–G) Example stromal immune cells showed either stationary cell bodies with processes that survey nearby vessels (E and F) and that retract following upon contacting a different immune cell (F) or, occasionally, cell body movement constrained by surrounding vessels (G).

(H) Left, middle: i.p.-injected red dextran (70 kDa) fills the ChP vasculature. Right: 2 days later, dextran has leaked into stromal space and accumulated within immune cells. Scale bar, 50 μm.

(I) Snapshots of dextran punctae accumulating within immune cell processes (arrowheads) in blue dashed box in (H). See also Figure S5; Video S14.

By developing tools for volumetric, multi-color two-photon imaging of vasculature and immune cells within and on the surface of the ChP *in vivo*, we uncovered spontaneous surveillance behaviors of immune cells as well as profound immune cell activation and translocation following peripheral or local perturbations. We hope this ChP imaging toolkit will accelerate the pace of discoveries regarding the diverse functions of this vital deep brain tissue.

Imaging the ChP *In Vitro* and *In Vivo*

The above methods for imaging ChP explants should be of broad utility, as this approach is relatively simple and inexpensive and allows tracking of tissue prior to and following controlled delivery of multiple drugs to the apical surface of the ChP. Our description of vascular landmarks should also improve repeatability

within and across studies. The LV ChP tissue is thin and delicate and not entirely flat (albeit much flatter than third and fourth ventricle ChP). Thus, in order to obtain high-quality data, it was important to carefully extract the explant, stably mount it, and adjust fluid flow and osmolarity to avoid undue stretch and pressure (Figure S1A).

In vivo methods enabled monitoring of ChP in a largely natural environment during systemic delivery of drugs or perturbations (Figures 4, 6, and 7). Although *in vivo* imaging using a cannula has been demonstrated in many deep brain areas (e.g., Dombeck et al., 2010; Liang et al., 2018), motion of ChP tissue posed a particularly challenging problem, as the ChP is anchored at the ventromedial aspect of the LV, far from the dorsal ChP regions that we imaged. This likely contributed to substantial non-rigid motion in three dimensions beyond what is observed in other brain tissues that are pressurized and anchored by the imaging window. Thus, although our use of a treadmill to minimize head torque applied by the limbs likely reduced motion artifacts to some extent (Dombeck et al., 2007), it was critical to additionally use several methods for two-dimensional (2D) and non-rigid 3D co-registration of imaging datasets in order to attain subcellular resolution (Figure 5). Another option to reduce coupling of body and brain

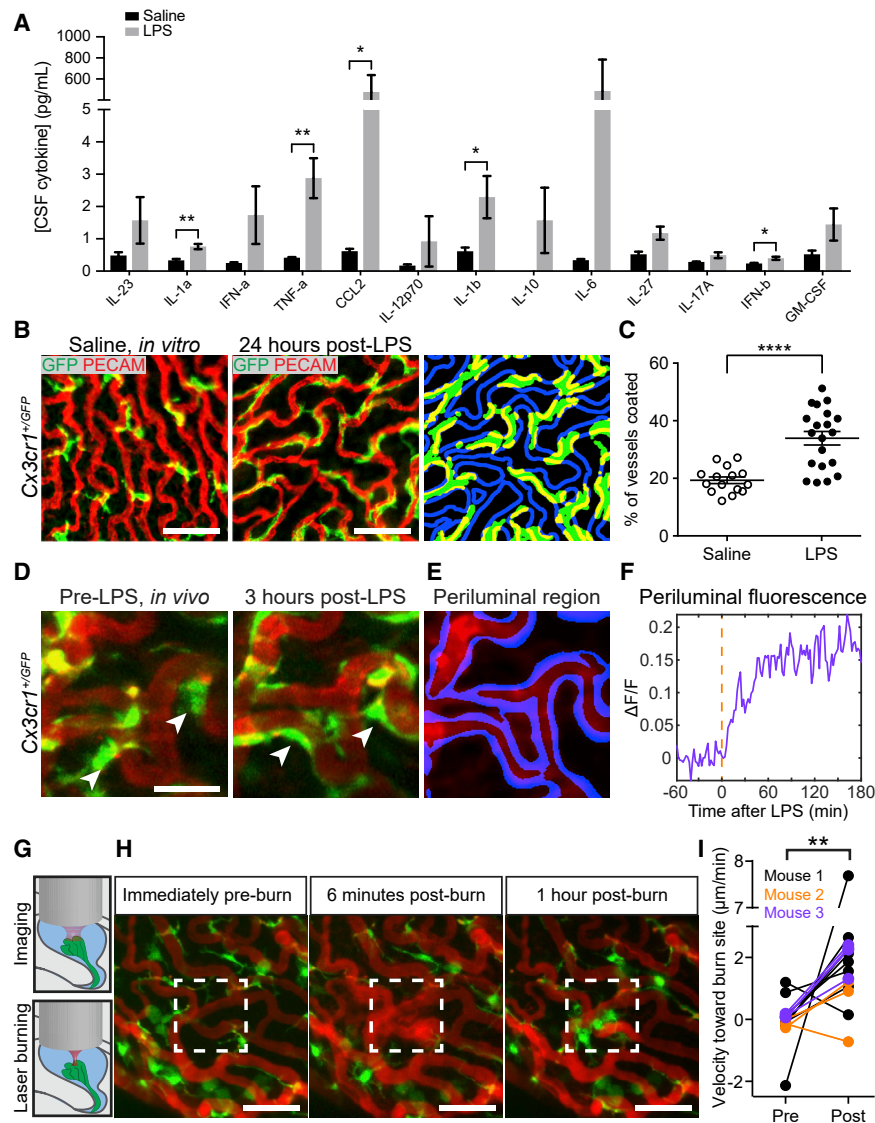


Figure 7. ChP Immune Cells Respond to Systemic and Local Insults

(A) Higher CSF cytokine levels 1 h after i.p. injection of LPS versus saline (mean \pm SEM; n = 3 samples, each consisting of 25 μ L pooled across three to six mice; IL-1 α , **p = 0.0017; TNF- α , **p = 0.0072; CCL2, *p = 0.0260; IL1 β , *p = 0.0451; and IFN- β , *p = 0.0212 [unpaired t tests]).

(B–D) Following LPS, immune cells flatten along vessels. (B) LV ChP explants from *Cx3cr1*^{+/GFP} mice that received i.p. saline (left) or LPS (middle). Segmentation of immune cells (right panel, green), and perivascular region surrounding vasculature (blue; Figures S6B and S6C; STAR Methods) allowed assessment of overlap (yellow). Scale bar, 50 μ m. (C) Percentage of perivascular region occupied by immune cell processes following i.p. saline (n = 15 explants, nine mice) or LPS (n = 20 explants, ten mice). ****p < 0.0001, Welch's t test. Mean \pm SEM. (D) *In vivo* imaging of immune cells (green) and vasculature (red) pre-LPS (left) and 3 h following i.p. LPS (right). Scale bar, 25 μ m. Arrowheads, transitions of cell bodies to splayed morphology (see Video S16).

(E) Segmentation of perivascular region (STAR Methods).

(F) Fractional change in immune cell fluorescence ($\Delta F/F$) in perivascular region across 4 h, relative to pre-LPS baseline (red line).

(G) Schematic of focal injury via brief, high-power focusing of a laser on a small region of ChP during *in vivo* imaging.

(H) Maximum projections of immune cells and vasculature before, 6 min after, and 1 h after a local burn within the white box. At 6 min, dextran leaks out of damaged vessels (see Video S17). Immune cell bodies then migrate to the injury site. Scale bar, 50 μ m.

(I) Average pre- and post-injury velocity of immune cells toward (positive) or away from (negative) the injury site (n = 15 cells, three mice). **p = 0.0075, paired t test.

motion could be to anesthetize mice prior to imaging. Although this may be particularly useful for structural imaging studies, anesthesia could significantly alter the functional properties of the ChP.

We did not observe sustained inflammation of ChP for time points at which imaging was performed, several weeks following implantation (Figure S3). Intracranial pressure also normalized to baseline levels following this recovery period (data not shown). This recovery period also improved imaging clarity in comparison with acute imaging immediately following surgery (not shown), consistent with deep imaging in other brain regions (Goldey et al., 2014; Liang et al., 2018). Nevertheless, additional improvements to our approach could further minimize the invasive nature of the cannula implant. For example, with improved red and infrared fluorescent indicators, window implants for two- and three-photon imaging of ChP can be placed well above the dorsal surface of the LV (e.g., Wang et al., 2018; Weisenburger et al., 2019). Alternatively, lower

profile GRIN lenses may be used for intraventricular imaging, albeit with a much smaller field of view and range of imaging depths.

Spontaneous and Evoked Calcium Activity and Vesicle Fusion in ChP

We observed diverse rates of spontaneous calcium activity and diverse thresholds for evoked activity across nearby cells. These differences may relate to differences in activity states or to subtypes of epithelial cells. In the future, such functional characterizations of epithelial cells can be merged with single-cell transcriptomics (Dani et al., 2019) to better understand potential divisions of labor across cells.

Spontaneous calcium transients were restricted to subregions of a cell. Future studies can assess whether these subcellular events relate to the subcellular vesicle fusion events we observed in explants or to activation of a single protrusion among the many protrusions on the apical surface of each

epithelial cell (evident in EM images in [Figure S2I](#)). These events were particularly fast (~200 ms) when measured *in vivo*, possibly because of calcium imaging at warmer ambient temperatures *in vivo* versus *in vitro*.

Application of a 5-HT_{2C} receptor agonist drove strong increases in calcium activity and increased rates of vesicular fusion. This calcium sensitivity of epithelial tissue to serotonin and associated agonists is consistent with previous reports using cultured, dissociated ChP cells ([Watson et al., 1995](#)). Higher concentrations of 5-HT_{2C} agonist evoked large, apocrine-type secretory events ([Figures 4L–4N](#); [Videos S9 and S10](#)) that have been reported in ChP and other epithelia, including sweat and mammary glands ([Farkaš, 2015](#)). Although these secretory events involve massive release of internal contents from an epithelial cell, they do not imply that cell health is compromised. Rather, this process may represent an efficient and rapid means for activity-dependent secretion of large amounts of cargo in response to an external stimulus, possibly in conjunction with other rapid changes (e.g., rapid activation of water and ion channels). Our studies set the stage for more in-depth investigations of how the ChP dynamically regulates the molecular composition of the CSF that bathes the CNS.

Immune Surveillance at the ChP

Immune cells have been proposed to enter the brain via the ChP ([Gherzi-Egea et al., 2018](#); [Reboldi et al., 2009](#); [Schwartz and Baruch, 2014](#); [Shechter et al., 2013](#)), but little is known about the functions of resident ChP immune cells during baseline conditions or in response to peripheral immune challenge or local injury. Tracking of *Cx₃cr₁*-expressing ChP immune cells together with vascular labeling *in vivo* revealed vascular surveillance by stromal immune cell processes, while cell bodies remained largely immobile. This surveillance points to active maintenance and phagocytic roles at the blood-CSF barrier. Notably, we found that these stromal immune cells still contained 70 kDa dextrans weeks after i.p. injection. In contrast, epilexus cells on the apical surface of the ChP showed much greater cell body mobility but did not take up dextrans.

ChP immune cells also responded to systemic LPS delivery by spreading their cell bodies and processes along the periluminal region near blood vessels, a finding confirmed using immunohistochemistry. This cellular response may reflect a means of protection against peripheral insults, and differs from that of cortical microglia, which retract their processes and adopt an amoeboid “activated” shape during inflammation ([Pozner et al., 2015](#)). Without access to the time-lapse *in vivo* imaging, it would not have been possible to determine whether the same local immune cells change their morphology and location or whether new immune cells had entered the same region of ChP. Indeed, despite previous reports that immune cells cross at the ChP ([Gherzi-Egea et al., 2018](#); [Reboldi et al., 2009](#); [Schwartz and Baruch, 2014](#); [Shechter et al., 2013](#)), our imaging sessions did not reveal arrival or departure of new immune cells from either the CSF or the vasculature during baseline conditions or following LPS. Future studies should examine deeper regions of the LV across a broader range of conditions to more fully assess potential subregions that mediate transit of immune cells to and from the brain.

We also noted rapid mobilization of nearby immune cells following deliberate heating of a focal region of the field of view using transient, high-magnification and high-power two-photon imaging. Many of these cells were epilexus cells, which acted as “first responders” by accumulating at the injury site. This behavior is strikingly different from that of *Cx₃cr₁*-positive microglia in cortex and other brain regions ([Davalos et al., 2005](#); [Pozner et al., 2015](#)), which extend their processes toward a laser-induced lesion to contain the injury while their cell bodies remain stationary ([Davalos et al., 2005](#)). Our findings can inform surgical procedures involving focal heating of ChP, such as during cauterization of ChP to treat hydrocephalus ([Warf, 2005](#)).

In the future, it should be possible to use the *in vivo* imaging approach described here to assess the role of changes in calcium and other intracellular signals in immune cells, epithelial cells, and other stromal cell types in the ChP during these and other immune challenges and brain injuries. A better understanding of the dynamic roles of multiple ChP cell types in various barrier functions in the intact brain should spark new ideas for penetrating this barrier for drug delivery to the brain, as well as for fortifying this barrier across the lifespan. More generally, given that repeated *in vivo* access and chronic imaging may be more amenable in the ChP than in most other body epithelia other than skin epithelium ([Mesa et al., 2015](#); [Rompolas et al., 2016](#)), this platform may provide a unique window into the general functions of barrier epithelia in their natural environments.

STAR★METHODS

Detailed methods are provided in the online version of this paper and include the following:

- KEY RESOURCES TABLE
- RESOURCE AVAILABILITY
 - Lead Contact
 - Materials Availability
 - Data and Code Availability
- EXPERIMENTAL MODEL AND SUBJECT DETAILS
- METHOD DETAILS
 - ChP explant preparation
 - In Vitro Epithelial Cell Experiments
 - Segmentation of cell masks
 - Trace extraction
 - *In vitro* two-photon calcium imaging
 - VAMP3-pHluorin imaging
 - *In Vivo* Imaging Experiments
 - *In Vivo* Epithelial Cell Experiments
 - Two-photon imaging of spontaneous activity
 - Registration/preprocessing of spontaneous activity
 - Cellular and subcellular segmentation – spontaneous activity
 - Subcellular trace extraction – spontaneous activity
 - *In vivo* 3D imaging of epithelial cell responses to delivery of a serotonin agonist
 - *In Vivo* Immune Cell Experiments
 - Two-photon imaging
 - 3D registration
 - Inter-volume motion artifacts

- Re-registration of single-cell regions
- Recording “physiological housekeeping” by immune cells
- Response to LPS
- Quantifying *in vitro* “vessel coating” by immune cells
- *In vivo* vessel coating
- Immune Cell Imaging During Acute Chp Injury
- Tracking immune cell acute response to laser burn injury
- Other Supporting Experiments
- Nearest-neighbor analysis
- Cytokine FACS array
- Quantitative RT-qPCR
- Transmission and Scanning EM
- **QUANTIFICATION AND STATISTICAL ANALYSIS**

SUPPLEMENTAL INFORMATION

Supplemental Information can be found online at <https://doi.org/10.1016/j.neuron.2020.08.024>.

ACKNOWLEDGMENTS

We thank members of the Lehtinen, Andermann, and Moore labs for helpful discussions; A. Lutas, K. Fernando, S. Marsh, M. Webb, C. Chen, O. Alturkistani, and the IDDRC Imaging Core for advice and technical assistance; M. Bhaumik, BCH Genome Editing Core, and G. Marsischky for *Htr2c^{mRuby3}* design; M. Ericsson, HMS EM Facility; W.H. Fowle, NEU EM Facility; C. Wu at the BCH Viral Core; S. Gupton for VAMP3 expression vector; and J. Zhang for Z310 cells. This work was supported by a National Science Foundation (NSF) Graduate Research Fellowship (F.B.S.); a Glenn Foundation/American Federation for Aging Research (AFAR) Postdoctoral Fellowship and a Reagan Sloane Shanley Research Internship (N.D.); a William Randolph Hearst Fellowship (N.D., J.C.); NIH grant T32 HL110852 (J.C., R.M.F.); an Office of Faculty Development (OFD)/Basic/Translational Research Executive Committee (BTREC)/Clinical and Translational Research Executive Committee (CTREC) Faculty Development Fellowship Award (R.M.F.); NIH National Institute of Allergy and Infectious Diseases (NIAID) grant R01-AI130591 (T. Kishkovich, K.H.); National Heart, Lung, and Blood Institute (NHLBI) grant R35-HL145242 (M.J.H.); GM075252 (T. Kirchhausen); a gift from the Korn family and NSF Next Generation Networks for Neuroscience (NeuroNex) grant 1707352 (C.I.M.); the David Mahoney Neuroimaging Grant Program – Dana Foundation, NIH grants DP2 DK105570, DP1 AT010971, R01 DK109930, R21 EY03043-02, the McKnight Foundation, the Pew Foundation, the Smith Family Foundation, the Klarman Family Foundation, and the AFAR (M.L.A.); the Pediatric Hydrocephalus Foundation, a Tommy Fuss Center Innovation Grant, Simons Foundation Autism Research Initiative [SFARI] award 610670, a Harvard Brain Science Initiative Bipolar Disorder Seed Grant, and NIH grant R01 NS088566 (M.K.L.); Human Frontier Science Program grant RGP0063/2018 (C.W., M.K.L.); NIH grant RF1DA048790 (C.I.M., M.K.L.); New York Stem Cell Foundation (NYSCF) grants NYSCF-R-NI39 (C.W.) and NYSCF-R-NI38 (M.K.L.); and Boston Children’s Hospital (BCH) Intellectual and Developmental Disabilities Research Center (IDDRC) grant 1U54HD090255. C.W. and M.K.L. are New York Stem Cell Foundation – Robertson Investigators. The content is solely the responsibility of the authors and does not necessarily represent the official views of the National Institutes of Health.

AUTHOR CONTRIBUTIONS

F.B.S., N.D., M.L.A., C.I.M., and M.K.L. designed the study. N.D. and F.B.S. developed whole-tissue explants and imaging protocols. C.D. and M.L.A. developed the *in vivo* two-photon calcium imaging protocol. F.B.S. performed all computational analyses of all imaging data with advice from M.L.A. J.C. helped generate *Htr2c^{mRuby3}* mice. F.B.S., J.C., and M.L.S. analyzed peripheral activation of immune cells. H.X. analyzed secretory pathways and devel-

oped the vesicle imaging assay with assistance from C.W., K.H., and T. Kirchhausen. J.H. developed immediate-early gene assays. G.J.G. developed and T. Kishkovich, E.J., E.K., V.I.F., and C.S. refined the imaging cannula approach. J.C. and R.M.F. analyzed CSF cytokines. Y.Z. and M.J.H. shared *FoxJ1-Cre* mice. F.B.S., M.L.A., and M.K.L. wrote the manuscript.

DECLARATION OF INTERESTS

The authors declare no competing interests.

Received: November 13, 2019

Revised: May 18, 2020

Accepted: August 25, 2020

Published: September 21, 2020

REFERENCES

- Agnew, W.F., Yuen, T.G., and Achtyl, T.R. (1980). Ultrastructural observations suggesting apocrine secretion in the choroid plexus: a comparative study. *Neurol. Res.* **7**, 313–332.
- Ambudkar, I.S. (2016). Calcium signalling in salivary gland physiology and dysfunction. *J. Physiol.* **594**, 2813–2824.
- Ambudkar, I. (2018). Calcium signaling defects underlying salivary gland dysfunction. *Biochim. Biophys. Acta Mol. Cell Res.* **1865** (11 Pt B), 1771–1777.
- Audhya, T., Adams, J.B., and Johansen, L. (2012). Correlation of serotonin levels in CSF, platelets, plasma, and urine. *Biochim. Biophys. Acta* **1820**, 1496–1501.
- Baddedy, A., Rubak, E., and Turner, R. (2015). *Spatial Point Patterns: Methodology and Applications with R* (Boca Raton, FL: Chapman and Hall/CRC Press).
- Balaji, R., Bielmeier, C., Harz, H., Bates, J., Stadler, C., Hildebrand, A., and Classen, A.-K. (2017). Calcium spikes, waves and oscillations in a large, patterned epithelial tissue. *Sci. Rep.* **7**, 42786.
- Balusu, S., Brkic, M., Libert, C., and Vandenbroucke, R.E. (2016a). The choroid plexus-cerebrospinal fluid interface in Alzheimer’s disease: more than just a barrier. *Neural Regen. Res.* **11**, 534–537.
- Balusu, S., Van Wouterghem, E., De Rycke, R., Raemdonck, K., Stremersch, S., Gevaert, K., Brkic, M., Demeestere, D., Vanhooren, V., Hendrix, A., et al. (2016b). Identification of a novel mechanism of blood-brain communication during peripheral inflammation via choroid plexus-derived extracellular vesicles. *EMBO Mol. Med.* **8**, 1162–1183.
- Cloutier, N., Paré, A., Farndale, R.W., Schumacher, H.R., Nigrovic, P.A., Lacroix, S., and Boilard, E. (2012). Platelets can enhance vascular permeability. *Blood* **120**, 1334–1343.
- Cocucci, E., Aguet, F., Boulant, S., and Kirchhausen, T. (2012). The first five seconds in the life of a clathrin-coated pit. *Cell* **150**, 495–507.
- Concepcion, A.R., and Feske, S. (2017). Regulation of epithelial ion transport in exocrine glands by store-operated Ca²⁺ entry. *Cell Calcium* **63**, 53–59.
- Conn, P.J., and Sanders-Bush, E. (1986). Agonist-induced phosphoinositide hydrolysis in choroid plexus. *J. Neurochem.* **47**, 1754–1760.
- Coulter, M.E., Dorobantu, C.M., Lodewijk, G.A., Delalande, F., Cianferani, S., Ganesh, V.S., Smith, R.S., Lim, E.T., Xu, C.S., Pang, S., et al. (2018). The ESCRT-III protein CHMP1A mediates secretion of sonic hedgehog on a distinctive subtype of extracellular vesicles. *Cell Rep.* **24**, 973–986.e8.
- Crossgrove, J.S., Li, G.J., and Zheng, W. (2005). The choroid plexus removes beta-amyloid from brain cerebrospinal fluid. *Exp. Biol. Med.* (Maywood) **230**, 771–776.
- Damkier, H.H., Brown, P.D., and Praetorius, J. (2013). Cerebrospinal fluid secretion by the choroid plexus. *Physiol. Rev.* **93**, 1847–1892.
- Dani, N., Herbst, R.H., Habib, N., Head, J., Dionne, D., Nguyen, L., McCabe, C., Cui, J., Shipley, F.B., Jang, A., et al. (2019). A cellular and spatial map of the choroid plexus across brain ventricles and ages. *bioRxiv*. <https://doi.org/10.1101/627539>.

- Davalos, D., Grutzendler, J., Yang, G., Kim, J.V., Zuo, Y., Jung, S., Littman, D.R., Dustin, M.L., and Gan, W.-B. (2005). ATP mediates rapid microglial response to local brain injury in vivo. *Nat. Neurosci.* **8**, 752–758.
- Doench, J.G., Fusi, N., Sullender, M., Hegde, M., Vaimberg, E.W., Donovan, K.F., Smith, I., Tothova, Z., Wilen, C., Orchard, R., et al. (2016). Optimized sgRNA design to maximize activity and minimize off-target effects of CRISPR-Cas9. *Nat. Biotechnol.* **34**, 184–191.
- Dombeck, D.A., Khabbaz, A.N., Collman, F., Adelman, T.L., and Tank, D.W. (2007). Imaging large-scale neural activity with cellular resolution in awake, mobile mice. *Neuron* **56**, 43–57.
- Dombeck, D.A., Harvey, C.D., Tian, L., Looger, L.L., and Tank, D.W. (2010). Functional imaging of hippocampal place cells at cellular resolution during virtual navigation. *Nat. Neurosci.* **13**, 1433–1440.
- Esterle, T.M., and Sanders-Bush, E. (1992). Serotonin agonists increase transferrin levels via activation of 5-HT_{1C} receptors in choroid plexus epithelium. *J. Neurosci.* **12**, 4775–4782.
- Fame, R.M., and Lehtinen, M.K. (2020). Emergence and developmental roles of the cerebrospinal fluid system. *Dev. Cell* **52**, 261–275.
- Farkaš, R. (2015). Apocrine secretion: new insights into an old phenomenon. *Biochim. Biophys. Acta* **1850**, 1740–1750.
- Gherzi-Egea, J.-F., Strazielle, N., Catala, M., Silva-Vargas, V., Doetsch, F., and Engelhardt, B. (2018). Molecular anatomy and functions of the choroidal blood-cerebrospinal fluid barrier in health and disease. *Acta Neuropathol.* **135**, 337–361.
- Goldy, G.J., Roumis, D.K., Glickfeld, L.L., Kerlin, A.M., Reid, R.C., Bonin, V., Schafer, D.P., and Andermann, M.L. (2014). Removable cranial windows for long-term imaging in awake mice. *Nat. Protoc.* **9**, 2515–2538.
- Gonzalez, A.M., Leadbeater, W.E., Burg, M., Sims, K., Terasaki, T., Johanson, C.E., Stopa, E.G., Eliceiri, B.P., and Baird, A. (2011). Targeting choroid plexus epithelia and ventricular ependyma for drug delivery to the central nervous system. *BMC Neurosci.* **12**, 4.
- Gudeman, D.M., Nelson, S.R., and Merisko, E.M. (1987). Protein secretion by choroid plexus: isolated apical fragments synthesize protein in vitro. *Tissue Cell* **19**, 101–109.
- Gudeman, D.M., Brightman, M.W., Merisko, E.M., and Merrill, C.R. (1989). Release from live choroid plexus of apical fragments and electrophoretic characterization of their synthetic products. *J. Neurosci. Res.* **24**, 184–191.
- Guizar-Sicairos, M., and Fienup, J.R. (2008). Direct image reconstruction from a Fourier intensity pattern using HERALDO. *Opt. Lett.* **33**, 2668–2670.
- Haddad, M.R., Donsante, A., Zervas, P., and Kaler, S.G. (2013). Fetal brain-directed AAV gene therapy results in rapid, robust, and persistent transduction of mouse choroid plexus epithelia. *Mol. Ther. Nucleic Acids* **2**, e101.
- Hickman, S., Izzy, S., Sen, P., Morsett, L., and El Khoury, J. (2018). Microglia in neurodegeneration. *Nat. Neurosci.* **21**, 1359–1369.
- Hierro-Bujalance, C., Bacskai, B.J., and Garcia-Alloza, M. (2018). In vivo imaging of microglia with multiphoton microscopy. *Front. Aging Neurosci.* **10**, 218.
- Hudry, E., and Vandenbergh, L.H. (2019). Therapeutic AAV gene transfer to the nervous system: a clinical reality. *Neuron* **101**, 839–862.
- Hudson, A.J. (1960). The development of the vascular pattern of the choroid plexus of the lateral ventricles. *J. Comp. Neurol.* **115**, 171–186.
- Jerman, T., Pernus, F., Likar, B., and Spiclin, Z. (2016). Enhancement of vascular structures in 3D and 2D angiographic images. *IEEE Trans. Med. Imaging* **35**, 2107–2118.
- Jung, S., Aliberti, J., Graemmel, P., Sunshine, M.J., Kreutzberg, G.W., Sher, A., and Littman, D.R. (2000). Analysis of fractalkine receptor CX₃CR1 function by targeted deletion and green fluorescent protein reporter gene insertion. *Mol. Cell. Biol.* **20**, 4106–4114.
- Karimy, J.K., Zhang, J., Kurland, D.B., Theriault, B.C., Duran, D., Stokum, J.A., Furey, C.G., Zhou, X., Mansuri, M.S., Montejo, J., et al. (2017). Inflammation-dependent cerebrospinal fluid hypersecretion by the choroid plexus epithelium in posthemorrhagic hydrocephalus. *Nat. Med.* **23**, 997–1003.
- Kierdorf, K., Masuda, T., Jordão, M.J.C., and Prinz, M. (2019). Macrophages at CNS interfaces: ontogeny and function in health and disease. *Nat. Rev. Neurosci.* **20**, 547–562.
- Kim, S., Hwang, Y., Lee, D., and Webster, M.J. (2016). Transcriptome sequencing of the choroid plexus in schizophrenia. *Transl. Psychiatry* **6**, e964.
- Lehtinen, M.K., Zappaterra, M.W., Chen, X., Yang, Y.J., Hill, A.D., Lun, M., Maynard, T., Gonzalez, D., Kim, S., Ye, P., et al. (2011). The cerebrospinal fluid provides a proliferative niche for neural progenitor cells. *Neuron* **69**, 893–905.
- Lein, E.S., Hawrylycz, M.J., Ao, N., Ayres, M., Bensinger, A., Bernard, A., Boe, A.F., Boguski, M.S., Brockway, K.S., Byrnes, E.J., et al. (2007). Genome-wide atlas of gene expression in the adult mouse brain. *Nature* **445**, 168–176.
- Li, Q., and Barres, B.A. (2018). Microglia and macrophages in brain homeostasis and disease. *Nat. Rev. Immunol.* **18**, 225–242.
- Liang, L., Fratzi, A., Goldey, G., Ramesh, R.N., Sugden, A.U., Morgan, J.L., Chen, C., and Andermann, M.L. (2018). A fine-scale functional logic to convergence from retina to thalamus. *Cell* **173**, 1343–1355.e24.
- Livak, K.J., and Schmittgen, T.D. (2001). Analysis of relative gene expression data using real-time quantitative PCR and the 2^{-ΔΔC_T} method. *Methods* **25**, 402–408.
- Lun, M.P., Johnson, M.B., Broadbelt, K.G., Watanabe, M., Kang, Y.J., Chau, K.F., Springel, M.W., Malesz, A., Sousa, A.M.M., Pletikos, M., et al. (2015a). Spatially heterogeneous choroid plexus transcriptomes encode positional identity and contribute to regional CSF production. *J. Neurosci.* **35**, 4903–4916.
- Lun, M.P., Monuki, E.S., and Lehtinen, M.K. (2015b). Development and functions of the choroid plexus-cerebrospinal fluid system. *Nat. Rev. Neurosci.* **16**, 445–457.
- Madisen, L., Garner, A.R., Shimaoka, D., Chuong, A.S., Klapoetke, N.C., Li, L., van der Bourg, A., Niino, Y., Egolf, L., Monetti, C., et al. (2015). Transgenic mice for intersectional targeting of neural sensors and effectors with high specificity and performance. *Neuron* **85**, 942–958.
- Marques, F., Sousa, J.C., Coppola, G., Falcao, A.M., Rodrigues, A.J., Geschwind, D.H., Sousa, N., Correia-Neves, M., and Palha, J.A. (2009). Kinetic profile of the transcriptome changes induced in the choroid plexus by peripheral inflammation. *J. Cereb. Blood Flow Metab.* **29**, 921–932.
- Marques, F., Sousa, J.C., Sousa, N., and Palha, J.A. (2013). Blood-brain-barriers in aging and in Alzheimer's disease. *Mol. Neurodegener.* **8**, 38.
- Mesa, K.R., Rompolas, P., Zito, G., Myung, P., Sun, T.Y., Brown, S., Gonzalez, D.G., Blagoev, K.B., Haberman, A.M., and Greco, V. (2015). Niche-induced cell death and epithelial phagocytosis regulate hair follicle stem cell pool. *Nature* **522**, 94–97.
- Monje, M.L., Toda, H., and Palmer, T.D. (2003). Inflammatory blockade restores adult hippocampal neurogenesis. *Science* **302**, 1760–1765.
- Mottahedin, A., Joakim Ek, C., Truvé, K., Hagberg, H., and Mallard, C. (2019). Choroid plexus transcriptome and ultrastructure analysis reveals a TLR2-specific chemotaxis signature and cytoskeleton remodeling in leukocyte trafficking. *Brain Behav. Immun.* **79**, 216–227.
- Mukamel, E.A., Nimmerjahn, A., and Schnitzer, M.J. (2009). Automated analysis of cellular signals from large-scale calcium imaging data. *Neuron* **63**, 747–760.
- Narboux-Nême, N., Pavone, L.M., Avallone, L., Zhuang, X., and Gaspar, P. (2008). Serotonin transporter transgenic (SERT^{Cre}) mouse line reveals developmental targets of serotonin specific reuptake inhibitors (SSRIs). *Neuropharmacology* **55**, 994–1005.
- Narciso, C.E., Contento, N.M., Storey, T.J., Hoelzle, D.J., and Zartman, J.J. (2017). Release of applied mechanical loading stimulates intercellular calcium waves in *Drosophila* wing discs. *Biophys. J.* **113**, 491–501.
- Netsky, M., and Shuangshoti, S. (1975). *The Choroid Plexus in Health and Disease* (New York: Elsevier).
- Okaty, B.W., Sturrock, N., Escobedo Lozoya, Y., Chang, Y., Senft, R.A., Lyon, K.A., Alekseyenko, O.V., and Dymecki, S.M. (2020). A single-cell transcriptomic and anatomic atlas of mouse dorsal raphe *Pet1* neurons. *eLife* **9**, e55523.

- Pellegrini, L., Bonfio, C., Chadwick, J., Begum, F., Skehel, M., and Lancaster, M.A. (2020). Human CNS barrier-forming organoids with cerebrospinal fluid production. *Science* 369, eaaz5626.
- Pozner, A., Xu, B., Palumbos, S., Gee, J.M., Tvrdik, P., and Capecchi, M.R. (2015). Intracellular calcium dynamics in cortical microglia responding to focal laser injury in the PC:G5-tdT reporter mouse. *Front. Mol. Neurosci.* 8, 12.
- Reboldi, A., Coisne, C., Baumjohann, D., Benvenuto, F., Bottinelli, D., Lira, S., Uccelli, A., Lanzavecchia, A., Engelhardt, B., and Sallusto, F. (2009). C-C chemokine receptor 6-regulated entry of TH-17 cells into the CNS through the choroid plexus is required for the initiation of EAE. *Nat. Immunol.* 10, 514–523.
- Rompolas, P., Mesa, K.R., Kawaguchi, K., Park, S., Gonzalez, D., Brown, S., Boucher, J., Klein, A.M., and Greco, V. (2016). Spatiotemporal coordination of stem cell commitment during epidermal homeostasis. *Science* 352, 1471–1474.
- Rosenzweig-Lipson, S., Zhang, J., Mazandarani, H., Harrison, B.L., Sabb, A., Sabalski, J., Stack, G., Welmaker, G., Barrett, J.E., and Dunlop, J. (2006). Antiobesity-like effects of the 5-HT_{2C} receptor agonist WAY-161503. *Brain Res.* 1073–1074, 240–251.
- Samanta, K., and Parekh, A.B. (2016). Store-operated Ca²⁺ channels in airway epithelial cell function and implications for asthma. *Philos. Trans. R. Soc. Lond. B Biol. Sci.* 371, 20150424.
- Sanders-Bush, E., and Breeding, M. (1990). Serotonin_{1c} receptor reserve in choroid plexus masks receptor subsensitivity. *J. Pharmacol. Exp. Ther.* 252, 984–988.
- Sankaranarayanan, S., De Angelis, D., Rothman, J.E., and Ryan, T.A. (2000). The use of pHLuorins for optical measurements of presynaptic activity. *Biophys. J.* 79, 2199–2208.
- Saunders, N.R., Dziegielewska, K.M., Møllgård, K., and Habgood, M.D. (2018). Physiology and molecular biology of barrier mechanisms in the fetal and neonatal brain. *J. Physiol.* 596, 5723–5756.
- Schwartz, M., and Baruch, K. (2014). The resolution of neuroinflammation in neurodegeneration: leukocyte recruitment via the choroid plexus. *EMBO J.* 33, 7–22.
- Shechter, R., Miller, O., Yovel, G., Rosenzweig, N., London, A., Ruckh, J., Kim, K.-W., Klein, E., Kalchenko, V., Bendel, P., et al. (2013). Recruitment of beneficial M2 macrophages to injured spinal cord is orchestrated by remote brain choroid plexus. *Immunity* 38, 555–569.
- Silva-Vargas, V., Maldonado-Soto, A.R., Mizrak, D., Codega, P., and Doetsch, F. (2016). Age-dependent niche signals from the choroid plexus regulate adult neural stem cells. *Cell Stem Cell* 19, 643–652.
- Stasi, C., Sadalla, S., and Milani, S. (2019). The relationship between the serotonin metabolism, gut-microbiota and the gut-brain axis. *Curr. Drug Metab.* 20, 646–655.
- Strazielle, N., and Gherzi-Egea, J.F. (1999). Demonstration of a coupled metabolism-efflux process at the choroid plexus as a mechanism of brain protection toward xenobiotics. *J. Neurosci.* 19, 6275–6289.
- Toda, T., Homma, D., Tokuoka, H., Hayakawa, I., Sugimoto, Y., Ichinose, H., and Kawasaki, H. (2013). Birth regulates the initiation of sensory map formation through serotonin signaling. *Dev. Cell* 27, 32–46.
- Tong, C.K., Chen, J., Cebrián-Silla, A., Mirzadeh, Z., Obernier, K., Guinto, C.D., Tecott, L.H., García-Verdugo, J.M., Kriegstein, A., and Alvarez-Buylla, A. (2014). Axonal control of the adult neural stem cell niche. *Cell Stem Cell* 14, 500–511.
- Urbina, F.L., Gomez, S.M., and Gupton, S.L. (2018). Spatiotemporal organization of exocytosis emerges during neuronal shape change. *J. Cell Biol.* 217, 1113–1128.
- Van Hove, H., Martens, L., Scheyltjens, I., De Vlaminc, K., Pombo Antunes, A.R., De Prijck, S., Vandamme, N., De Schepper, S., Van Isterdael, G., Scott, C.L., et al. (2019). A single-cell atlas of mouse brain macrophages reveals unique transcriptional identities shaped by ontogeny and tissue environment. *Nat. Neurosci.* 22, 1021–1035.
- Wang, T., Ouzounov, D.G., Wu, C., Horton, N.G., Zhang, B., Wu, C.H., Zhang, Y., Schnitzer, M.J., and Xu, C. (2018). Three-photon imaging of mouse brain structure and function through the intact skull. *Nat. Methods* 15, 789–792.
- Warf, B.C. (2005). Comparison of endoscopic third ventriculostomy alone and combined with choroid plexus cauterization in infants younger than 1 year of age: a prospective study in 550 African children. *J. Neurosurg.* 103 (6, Suppl), 475–481.
- Watanabe, M., Kang, Y.J., Davies, L.M., Meghpara, S., Lau, K., Chung, C.Y., Kathirya, J., Hadjantonakis, A.K., and Monuki, E.S. (2012). BMP4 sufficiency to induce choroid plexus epithelial fate from embryonic stem cell-derived neuroepithelial progenitors. *J. Neurosci.* 32, 15934–15945.
- Watson, J.A., Elliott, A.C., and Brown, P.D. (1995). Serotonin elevates intracellular Ca²⁺ in rat choroid plexus epithelial cells by acting on 5-HT_{2C} receptors. *Cell Calcium* 17, 120–128.
- Weisenburger, S., Tejera, F., Demas, J., Chen, B., Manley, J., Sparks, F.T., Martinez Traub, F., Daigle, T., Zeng, H., Losonczy, A., et al. (2019). Volumetric Ca(2+) imaging in the mouse brain using hybrid multiplexed sculpted light microscopy. *Cell* 177, 1050–1066.e14.
- Zhang, Y., Huang, G., Shornick, L.P., Roswit, W.T., Shipley, J.M., Brody, S.L., and Holtzman, M.J. (2007). A transgenic FOXJ1-Cre system for gene inactivation in ciliated epithelial cells. *Am. J. Respir. Cell Mol. Biol.* 36, 515–519.
- Zheng, W., and Zhao, Q. (2002). Establishment and characterization of an immortalized Z310 choroidal epithelial cell line from murine choroid plexus. *Brain Res.* 958, 371–380.
- Zheng, W., Zhao, Q., and Graziano, J.H. (1998). Primary culture of choroidal epithelial cells: characterization of an in vitro model of blood-CSF barrier. *In Vitro Cell. Dev. Biol. Anim.* 34, 40–45.

STAR★METHODS

KEY RESOURCES TABLE

REAGENT or RESOURCE	SOURCE	IDENTIFIER
Antibodies		
Mouse monoclonal anti-ACTA2-Cy3	Sigma-Aldrich	#C6198, RRID: AB_476856
Mouse monoclonal anti-AQP1	Santa Cruz	#sc-32737; RRID: AB_6266923
Rat monoclonal anti-CD31	BD Pharmingen	#550274, RRID: AB_393571
Chicken polyclonal anti-GFP	Abcam	#ab13970; RRID: AB_300798
Rabbit polyclonal anti-VAMP3	Synaptic System	#104103; RRID:AB_887812
Rabbit polyclonal anti-Iba1	Wako	#019-19741; RRID:AB_839504
Rabbit polyclonal anti-GFAP	Dako	#Z0334; RRID:AB_10013382
Rabbit polyclonal anti-S100 β	Dako	#Z0311; RRID:AB_10013383
Bacterial and Virus Strains		
pAAV-VAMP3-pHluorin	VAMP3-pHluorin coding sequence donated by Stephanie Gupton (Urbina et al., 2018)	N/A
Chemicals, Peptides, and Recombinant Proteins		
WAY-161503 hydrochloride	Tocris	#1801
Serotonin hydrochloride	Sigma	#H9523
Dextran, Texas Red, 70,000 MW Neutral	Life Technologies	#D1830
Lipopolysaccharide	Sigma	#L3024
Alt-R CRISPR Cas9 Nuclease V3	Integrated DNA Technologies	#1081060
HBSS	Fisher	#SH30031FS
Isoflurane	Patterson Veterinary	#07-893-2374
Meloxicam (NSAID analgesic)	Patterson Veterinary	#07-893-5916
Saline		N/A
Critical Commercial Assays		
TaqMan Fast Universal PCR Master Mix Gene Expression Assay	Thermo Fisher	#4366072
LEGENDplex Mouse Inflammation Panel (13-plex) w/ VbP	Biolegend	#740446
EndoFree Plasmid Maxi Kit	QIAGEN	#12362
miRNA isolation kit	mirVana	AM1560
Experimental Models: Cell Lines		
Z310 cells	(Zheng and Zhao, 2002)	N/A
Experimental Models: Organisms/Strains		
FoxJ1-CRE	(Zhang et al., 2007)	N/A
Cx3cr1-GFP	Jackson Laboratory	005582; RRID:IMSR_JAX:005582
Ai95D(RCL-GCaMP6f)-D	Jackson Laboratory	028865; RRID:IMSR_JAX:028865
Htr2C ^{mRuby3}	This paper	N/A
CD-1	Charles River	N/A
C57BL/6	Jackson Laboratory	000664; RRID:IMSR_JAX:000664
Oligonucleotides		
<i>c-fos</i> ; Mm00487425_m1	Thermo Fisher	Mm00487425_m1; #4453320
<i>Snap23</i> ; Mm01330351_mH	Thermo Fisher	Mm01330351_mH; #4448892
<i>Stx12</i> ; Mm00505689_m1	Thermo Fisher	Mm00505689_m1; #4448892
<i>Stxbp4</i> ; Mm00488497_m1	Thermo Fisher	Mm00488497_m1; #4448892
<i>Vamp3</i> ; Mm01268442_g1	Thermo Fisher	Mm01268442_g1; #4448892

(Continued on next page)

Continued		
REAGENT or RESOURCE	SOURCE	IDENTIFIER
Vamp2; Mm01325243_m1	Thermo Fisher	Mm01325243_m1; #4448892
Vmat2; Mm00553058_m1	Thermo Fisher	Mm00553058_m1; #4448892
c-fos; Mm00487425_m1	Thermo Fisher	Mm00487425_m1; #4453320
18S; Mm03928990_g1	Thermo Fisher	Mm03928990_g1; #4331182
crRNA Alt-R® CRISPR-Cas9 crRNA, 2 nmol	Integrated DNA Technologies	N/A
Software and Algorithms		
MATLAB R2018b	Mathworks	https://www.mathworks.com/products/matlab.html
Custom 3D registration algorithm	This paper	https://github.com/LehtinenLab/ShipleY2020
Vascular segmentation algorithm	This paper	https://github.com/LehtinenLab/ShipleY2020
Fiji 1.52i	NIH	https://fiji.sc/ RRID:SCR_002285
Scanbox	NeuroLabware	https://scanbox.org/
GraphPad Prism7	GraphPad Software Inc	https://www.graphpad.com/scientific-software/prism/
MicroManager	NIH	https://micro-manager.org
RStudio 1.2.5019	RStudio, Inc	https://rstudio.com
Spatstat R package	(Baddy et al., 2015)	https://spatstat.org/
FV31S-SW - FluoView	Olympus	https://www.olympus-lifescience.com/en/support/downloads/
LegendPlex v7.1	Biolegend	https://www.biolegend.com/en-us/legendplex
Other		
25x, 0.95 NA, 8mm W.D. objective	Olympus	XLPLN25XSVMP2
25x, 1.00 NA, 4mm W.D. objective	Olympus	XLPLN25XSVMP2
4x, 0.28 NA objective	Olympus	XLFLUOR 4x/340
100x, 1.46 NA objective	Carl Zeiss Microscopy	420792-9800-000
Dissection microscope	Carl Zeiss Microscopy	3715211/3715298
Confocal microscope with Airyscan	Carl Zeiss Microscopy	LSM 880
TIRF microscope	Intelligent Imaging Innovations, Inc	Marianas
Two-photon microscope	NeuroLabware	http://neurolabware.com/
IR cutoff filter – 775nm	Semrock	FF775-Di01-25x36
Red/green emission dichroic – 562 nm	Semrock	FF562-Di03-25x36
Green emission filter – 510 nm center, 84 nm width	Semrock	FF01-510/84-50
Red emission filter – 607 nm center, 70 nm width	Semrock	FF01-607/70
Two-photon microscope	Bruker	https://www.bruker.com/
Excitation dichroic mirror	Chroma	Z470/561/NIR-Trans
NIR blocker – block 458-473 nm, 561-568 nm	Chroma	Custom
Emission dichroic mirror – 560 nm	Chroma	T560lpxr
Blue/green emission dichroic mirror – 495 nm	Chroma	AT495lp
Green emission filter – 525 nm center, 50 nm width	Chroma	ET595/50
Two-photon microscope	Olympus	FVMPE-RS
IR cutoff filter – 685nm	Olympus	BA685
Excitation dichroic mirror	Olympus	FV30-SDM-M
Red/green Emission dichroic mirror – 570 nm	Olympus	SDM570
Green emission filter – 518 nm center, 45 nm width	Olympus	BA575-645
Red emission filter – 610 nm center, 70 nm band.	Olympus	BA495-540
Nanopositioning Piezo Stage	nPoint	nPFocus250
Tunable focus lens	Optotune	https://www.optotune.com/products/focus-tunable-lenses

(Continued on next page)

Continued

REAGENT or RESOURCE	SOURCE	IDENTIFIER
CCD Camera	Photometrics	QuantEM:512SC
SCMOS Camera	Hamamatsu	OrcaFlash 4.0LT
CCD Camera	Andor	Andor iXon Ultra
Ti:Sapphire laser	Spectra-Physics	Mai Tai HP DeepSee
Blackout fabric	Thorlabs	Cat#BK5
Coverglass 15 mm	Warner	SteREO Discovery.V8
Ultra Quiet Imaging Chamber, high profile, wide bath (Model #JG-23W/HP)	Warner	#64-0703
Heater controller single channel	Warner	#64-1487
Tygon tubing E-3603 (1.59mm ID x 3.18mm OD x 50ft)	VWR	#64-0100 (TC-324B)
Luer connector kit	Harvard Apparatus	89403-846
Water bath for preheating solutions (2 Liter)	VWR	72-1407
Polycarbonate membrane Nucleopore; 13 mm wide; 8.0 μm pore size	Whatman	#110414
Stereotaxic frame	KOPF	Model 940
Heating pad	CWE	Model TC-1000
Gelfoam	Moore Medical	#2928
Titanium headpost	HE Parmer (Goldey et al., 2014)	Custom
Stainless steel cannula	MicroGroup	Custom
Round cover glass; 3 mm	Harvard Apparatus	Cat#64-0720
UV-cured adhesive	Norland Products	Cat#7106
Vetbond	3M	Cat#1469SB
C&B Metabond	Parkell	Cat#S380
Silicone (Kwik-sil)	WPI	#600022

RESOURCE AVAILABILITY**Lead Contact**

Further information and requests for resources and reagents should be directed to and will be fulfilled by the Lead Contact, Maria Lehtinen (maria.lehtinen@childrens.harvard.edu).

Materials Availability

All unique/stable reagents generated in this study are available from the Lead Contact with a completed Materials Transfer Agreement.

Data and Code Availability

The registration and vascular segmentation algorithms generated for this study are available at <https://github.com/LehtinenLab/ShipleY2020>. Original data are available from the Lead Contact upon request.

EXPERIMENTAL MODEL AND SUBJECT DETAILS

All animal care and experimental procedures were approved by the Institutional Animal Care and Use Committees of Beth Israel Deaconess Medical Center (Figures 3, 5, 6, and 7), Boston Children's Hospital (Figures 1, 2, 3, 4, 5, 6, and 7), and Brown University (Figures 3 and 4). Mouse lines used include *FoxJ1-Cre* (Zhang et al., 2007), *Ai95D* (Jax# 024105; Madisen et al., 2015), *Cx₃cr₁^{+/-GFP}* (Jax# 005582; Jung et al., 2000), *Htr2C^{mRuby3}*, CD-1, and C57BL/6 (Figures 1 and 2: male and female mice; Figures 3, 4, 5, 6, and 7 male mice). *Htr2C^{mRuby3}* mice were generated by the Gene Manipulation & Genome Editing Core, IDDR, BCH. Best-ranked sgRNAs near the targeting region in *Htr2C* genome were picked (Doench et al., 2016) and synthesized (Alt-R[®] CRISPR-Cas9 crRNA, Integrated DNA Technologies). Donor plasmid was custom made at GeneScript, prepared with EndoFree Plasmid Maxi Kit (QIAGEN). Alt-R[®] S.p. HiFi Cas9 Nuclease (Integrated DNA Technologies) was used for the editing. A mixture of crRNA (0.61 μM), Cas9 protein (10 ng/μl), and donor (10ng/μl) was injected into 0.5 dpc embryos harvested from C57BL/6NHsd (Envigo) mating pairs. Embryos that

survived the injection were implanted into recipient pseudopregnant females and allowed to reach term. Tail biopsies from pups were genotyped to identify founders. The line was maintained in C57BL/6J.

METHOD DETAILS

ChP explant preparation

Whole ChP from the lateral ventricle was harvested using #5 forceps and fine-dissection scissors. To collect the LV ChP, the hind-brain was separated from the mid- and forebrain structures using a scalpel, followed by a bilateral cut along the midline to separate the cortex into two hemispheres. Each hemisphere was stabilized with forceps and a third of the rostral end was cut off, the developing hippocampus was rolled out using the flat surface of a scalpel, and the attached LV ChP was gently separated from the hippocampus/fornix using forceps.

LV ChP was transferred onto round coverslips (15 mm, Warner Instruments, Cat. 64-0733) that had been prepared as follows: briefly, coverslips were lightly coated with Silicone (Kwik-sil, World Precision Instruments, Item. 600022), and while wet (1x aCSF: 119 mM NaCl, 2.5 mM KCl, 26 mM NaHCO₃, 1 mM NaH₂PO₄, 11 mM glucose, with fresh 2.0 mM magnesium chloride and 2.8 mM calcium chloride), a polycarbonate membrane (Whatman, Nucleopore, 13 mm wide, 8.0 μm pore size, Cat. 110414) was placed on the coverslip. Edges of the polycarbonate membrane were attached to the coverslip using adhesive (3M, Vetbond). These glass coverslips were kept at room temperature and allowed to cure. The ChP was flattened onto the membrane and secured using 3M Vetbond. All samples were placed in a holding chamber with continuously oxygenated (95% O₂ / 5% CO₂) 1x aCSF.

In Vitro Epithelial Cell Experiments

In vitro epifluorescence calcium imaging

Epifluorescence calcium recordings were acquired from *FoxJ1-Cre::Ai95D* ChP explants (see above) using a 4x, 0.28 NA objective (Olympus). A halogen lamp and FITC filter set (Olympus) were used for excitation and emission filtering. Green fluorescence was collected using an sCMOS camera (Hamamatsu). Images (2048 × 2048 pixels, 3.30 × 3.30 mm²) were acquired at 10 frames/s using MicroManager (NIH).

Segmentation of cell masks

Epifluorescence calcium videos were cropped to a small region (161 × 161 μm²) near the center of the sample, for ease of processing. We obtained cell masks based on cell shape, as follows: first, a mean image, I , was generated, and was locally contrast-normalized using:

$$I_n = \frac{I - G(I; \sigma=3)}{\sqrt{G(I; \sigma=3)}}$$

Where G is the 2D Gaussian operation. The normalized image was then binarized and watershed to separate cells that were joined together. Objects smaller than 5 pixels were considered noise and discarded. The convex hulls of remaining objects were used as cell masks. Neuropil masks were estimated as the annulus spanning the region between the cell perimeter and the perimeter obtained after dilating the cell by 5 pixels.

Trace extraction

A raw trace, $F(t)$, was extracted from each cell mask by calculating mean intensity across pixels in each mask, and for each movie frame. A neuropil activity trace, $F_{neuropil}(t)$, was calculated in the same way, using the corresponding neuropil mask. A neuropil-corrected signal, $F_{corrected}(t)$, was calculated by subtracting the neuropil trace from the raw trace, and adding back the mean of the signal:

$$F_{corrected} = F - F_{neuropil} + \bar{F}$$

The signal was further normalized by:

$$\Delta F/F = \frac{F_{corrected} - \text{median}(F_{corrected}, 500)}{\text{median}(F_{corrected}, 500)}$$

Where $\text{median}(F_{corrected}, 500)$ denotes a moving median filter with a window size of 500 frames (50 s) surrounding the time t .

Calcium events were defined as peaks in which $\Delta F/F > (5 \times \text{std}(\Delta F/F))$. Cells with traces that never exceeded this threshold were considered “inactive.”

In vitro two-photon calcium imaging

Two-photon microscopy was used to record calcium activity in explants in which ChP epithelial cells express GCaMP6f (in *FoxJ1-Cre::Ai95D* mice, using an Olympus MPE-RS two-photon microscope; 30.0 frames/s; 512x512 pixels/frame). All imaging was performed with a 25x, 1.0 NA objective (Olympus) at 4.5x digital zoom (~113 × 113 μm²). Laser power measured below the objective at 940 nm was 55 mW using a Mai Tai DeepSee laser (Spectra-Physics). To perform 3D recordings, the settings above were used

in conjunction with a nPFocus250 piezo microscope stage (nPoint) moving axially in a sawtooth pattern. 3D volume recordings were acquired at ~0.25 Hz to capture baseline activity, during which time aCSF flowed through the perfusion chamber (Warner; performed at room temperature) containing the ChP explant. Subsequently, increasing concentrations of 5-HT or the 5-HT_{2C} selective agonist, WAY-161503 (Tocris), in aCSF were introduced for one minute per concentration, with ten minute aCSF washouts in between drug deliveries. To measure bulk tissue fluorescence, a mean volume projection along the axial (z) dimension was performed to flatten each 3D volume into a 2D image, resulting in a 2D video across time. Average fluorescence across the 10 minutes baseline period prior to the first drug delivery was used as a baseline image. A ΔF image stack was constructed by subtracting this baseline image from each frame in the video. A trace of ΔF activity was calculated as the mean pixel intensity of each frame of the image stack.

VAMP3-pHluorin imaging

Cultured cells

Z310 cells were cultured on glass coverslips and lipofectamine transfected with pAAV-VAMP3-pHluorin. After 3 days, the cells were imaged using TIRF microscopy (Cocucci et al., 2012) with a 100x objective (1.46 NA, Carl Zeiss) and a 2x magnification lens placed in front of the CCD camera (QuantEM, Photometrics). This arrangement provided a final pixel size of 80 nm. ChP explants: AAV2/5-VAMP3-pHluorin was injected in utero i.c.v. in E14.5 embryos. LV ChP explants were then harvested at P18-P24. Each ChP was attached directly onto an imaging dish using Vetbond and immersed with 1.8 mL of aCSF. WAY-161503 was added until the final bath concentration reached 500 nM. Individual epithelial cells from explants were imaged using a ZEISS LSM880 Airyscan confocal microscope. The chamber, imaging dish holder, and all buffers used were maintained at 37°C.

To detect secreted vesicles, each image frame was first smoothed with a two-pixel radius Gaussian filter (160 nm). We then further filtered each image by calculating the determinate of the Hessian matrix at every pixel, and this image stack was used to isolate VAMP3 fusion events from cell background. Masks of regions involving a fusion event were obtained by PCA/ICA segmentation (Mukamel et al., 2009). Fluorescent traces were extracted by averaging fluorescence of all pixels within each mask. Each fluorescence trace was normalized to peak fluorescence, and sorted the traces by the time at which this peak occurred, in order to generate a heatmap of time courses of vesicle release events.

In Vivo Imaging Experiments

Headpost and cranial window placement

Mice used for *in vivo* two-photon imaging (8–20 weeks) were outfitted with a headpost (titanium, 0.7 g, H.E. Parmer) and 3 mm cranial window using minor modifications of techniques previously described (Goldey et al., 2014; Liang et al., 2018). Briefly, each cranial window implant was first prepared by gluing a 3 mm x 2 mm (diameter x height) stainless steel cylindrical cannula (MicroGroup) to a 3 mm diameter glass coverslip (Warner) using a UV-cured optical adhesive (Norland, type 71). Approximately 3 hours prior to surgical implantation, dexamethasone sodium phosphate (4 mg/ml, intramuscular) was administered in order to reduce brain edema. Anesthesia was induced using isoflurane (1%–3% in 100% O₂, with flow rate titrated to a respiratory rate of 1 breath per minute). Using standard aseptic techniques and a stereomicroscope, a 3-mm diameter craniotomy was performed over the left side of the skull, centered using stereotactic coordinates (2.0 mm lateral and 0.2 mm posterior to Bregma). Next, portions of neocortex, corpus callosum, and hippocampal tissue were carefully and slowly aspirated to expose the lateral ventricle, with the specific purpose of preventing undue increase in intracranial pressure. The ChP was visualized floating within the ventricle. Hemostasis was achieved with copious irrigation using sterile phosphate-buffered saline and occasional use of gelfoam. At this point, the cranial window implant was inserted through the craniotomy site and lowered to a depth of approximately 2.0 mm below the skull where it pressed lightly on the surface of the thalamus and preserved direct visualization of the intact ChP. The cannula was temporarily affixed to the skull with Vetbond (3M) followed by a permanent seal with C&B Metabond (Parkell). A custom two-pronged titanium headpost was then affixed to the skull and again sealed with C&B Metabond (the headpost implantation can also be performed prior to the craniotomy according to investigator preference).

To create a low-profile adaptor to accommodate the water-immersion objective and light shielding, a custom 3D-printed imaging well (outer diameter of the base, inner diameter, height: 20 mm, 10 mm, 4 mm, or 7.5 mm, 5 mm, 1 mm) was then positioned around the cannula and glued to the cement and headpost. Animals were given Meloxicam (5 mg/kg, s.c.), individually housed, and allowed at least 2 weeks to recover before live imaging. The estimated success rate in obtaining clear windows was ~80% for a trained surgeon. In the first post-operative week, the mice were undisturbed and, during the second week, the mice were habituated to the imaging environment. Each mouse was placed on a custom 3D-printed running wheel and the animal's head was fixed using clamps (Thorlabs) that attach to each prong of the two-pronged titanium headpost. The running wheel and associated flexible hinges were useful for decreasing brain motion, by decreasing the degree to which hindlimb-related forces couple to brain motion. During two-photon imaging sessions, the low-profile imaging well was covered with blackout fabric (Thorlabs).

In Vivo Epithelial Cell Experiments

Epifluorescence imaging

To initially localize the ChP and assess stability and orientation of the ChP post-surgery, an epifluorescence video was recorded while scanning axially through the tissue. To account for lensing effects from changing z planes, planes were registered with scaled rotations to each other using the StackReg plugin in Fiji (NIH).

Two-photon imaging of spontaneous activity

To capture high-speed subcellular and cellular activity in epithelial cells *in vivo*, two-photon microscopy was used to record calcium activity in a ~25 cells. Imaging of GCaMP6f-expressing epithelial cells (in *FoxJ1-Cre::Ai95D* mice, see above) was performed using a resonant-scanning two-photon microscope (Olympus, 512x512 pixels/frame; Bruker, 490x 372 pixels/frame). Spontaneous activity was recorded at a single imaging plane (Olympus, 30.0 frames/s; Bruker 41.5 frames/s). All imaging was performed with a 25x, 1.0 NA objective (Olympus) at 4.5x digital zoom (~113 × 113 μm²). Laser power measured below the objective was 55 mW using a Mai Tai DeepSee laser at 940 nm (Newport Corp.).

Registration/preprocessing of spontaneous activity

To compensate for rapid ChP motion caused by mouse locomotion and changes in posture, each frame was registered to a target image created by the mean of the first 500 frames. Registration was performed by cross-correlating the Fourier transform of each image with this target image (i.e., rigid-body translation correction; [Guizar-Sicairos and Fienup, 2008](#)).

Cellular and subcellular segmentation – spontaneous activity

After registration, a mean image across the entire recording was generated. Cell outlines and outlines of cell nuclei were manually drawn for each cell in the field of view (~20–40 cells). Cytoplasm masks were generated from the difference between cell mask and nucleus mask. Cytoplasm masks were subdivided into 12 radially symmetric subsections from the center of the nucleus. The neuropil area was an annulus surrounding the cell, calculated by dilating the cytoplasm masks by 10 pixels, and excluding pixels in the original cell mask from this dilated cell mask.

Subcellular trace extraction – spontaneous activity

First, the aligned video was down-sampled by a factor of 4. For each cell, the raw sector activity (i.e., a pie slice of the cell), $F_{raw}(\theta, t)$, was calculated as mean activity across pixels inside each of the cytoplasm sectors (θ) for every time point, t . Neuropil activity, $F_{neuropil}(t)$ was calculated as mean pixel activity in the neuropil mask defined above, at every time point, t . Neuropil activity was subtracted from raw activity to generate a neuropil-corrected time course:

$$F_{corrected}(\theta, t) = F_{raw}(\theta, t) - F_{neuropil}(t)$$

To normalize for different baseline section brightness, a rolling median of 6.67 s was subtracted from neuropil-subtracted signal:

$$\Delta F(\theta, t) = F_{corrected}(\theta, t) - \text{median}_{\Delta t = 6.67s}(F_{corrected}(\theta, t))$$

To find subcellular calcium events, the maximum signal across cell sectors was calculated, for each time t , by taking a maximum projection across sectors, and then subtracting the median across sectors:

$$F_{max}(t) = \max_{\theta}(\Delta F(\theta, t))$$

$$\Delta F_{max}(t) = F_{max}(t) - \text{median}_t(F_{max}(t))$$

This approach generated a single trace of the largest fluorescence deviation from median fluorescence across cell sectors at every time point.

To identify subcellular events, a peak detector was applied to the above trace using a threshold based on the trace of median activity across sectors ('median trace', F_{med}). First, F_{med} was calculated as:

$$F_{med}(t) = \text{median}_{\theta}(\Delta F(\theta, t))$$

$$\Delta F_{med}(t) = F_{med}(t) - \text{median}_t(F_{med}(t))$$

Subcellular calcium events were defined as local peaks of epochs in which $\Delta F_{max} > (5 \times \text{std}(\Delta F_{med}(t)))$.

In vivo 3D imaging of epithelial cell responses to delivery of a serotonin agonist

To perform 3D recordings, the same imaging settings described above for spontaneous *in vivo* calcium imaging were used, but with the addition of a nPFocus250 piezo microscope stage (nPoint) that moved the imaging plane axially in a sawtooth pattern (scanning of 93 planes per volume across 350 μm of depth with a scan rate of frame rate of 30.0 frames/s, 512x512 pixels/frame, resulting in volume scanning of a 170x170x350 μm³ volume at 0.32 volumes/s).

To register these volumes, we first averaged together every ten volumes in order to improve signal-to-noise ratio. Since the observed effects of WAY-161503 were slow and long lasting, this approach did not overly compromise temporal resolution. Each plane of these average volumes was registered to the center z plane (middle plane) of the volume using the StackReg plugin in Fiji (NIH), creating a rectified volume. The maximum intensity projection of each of these rectified volumes were used to correct for inter-volume motion X-Y motion. Using the first volume as an anchor point, each volume was registered to the previous volume.

X-Y plane transverse shifts were calculated by cross-correlating the Fourier transformations of the maximum intensity projection of a given volume and of the previous volume (Guizar-Sicairos and Fienup, 2008).

In Vivo Immune Cell Experiments

Dextran injection

Mice received intraperitoneal injections of dextran conjugated with Texas Red (70 kDa, 0.2 mg/g i.p.). ThermoFisher Scientific), delivered 30 minutes before imaging. Presence of dextran in vasculature was confirmed by two-photon imaging.

Two-photon imaging

3D volume recording was necessary to robustly track the ChP across long timescales due to mouse motion, changes in posture, and occasional axial drift of ChP. Two-photon imaging of immune cells and vasculature was performed using a resonant-scanning two-photon microscope (experiments were performed on two different microscopes: Olympus; 12.8 frame/s; 512 × 512 pixels/frame; 0.16 volumes/s, 81 planes/volume; volume size: 254 × 254 × 400 μm³. Neurolabware: 15.5 frames/s; 796 × 512 pixels/frame; 0.25–0.5 volumes/s, 31–62 planes/volumes; volume size: 355 × 230 × 100 μm³). Volume scanning on the Olympus was achieved by using a piezo microscope stage (nPFocus250). Volume scanning on the Neurolabware microscope was achieved using a tunable focus lens (Optotune). All imaging was performed with a 25x, 0.95 NA objective (Olympus) at 2x zoom (~254 × 254 μm² (Olympus), ~360 × 230 μm² (Neurolabware)). Laser power at 940–960 nm (Mai Tai DeepSee laser, Spectra Physics) measured below the objective was 30–40 mW. Immune cells were confirmed to be located within or on the outside of the ChP based on colocalization with the fluorescent dextran-labeled vasculature pattern.

3D registration

Due to the rapid motility of immune cells across seconds, 3D registration of individual volumes was necessary to properly account for ChP movement at these rapid timescales (see Figure 5). To account for optical deformation and warping caused by the focus-tunable lens, a counter-warping correction was calculated for each imaging session. The first 30 volumes were averaged together to create a mean distorted volume. The affine transformation was used to iteratively match each plane to its neighbor, beginning with the brightest plane of the volume and moving up and down until the ends of the volume. Since affine transformations are linear functions, the adjacent transformations could be combined by multiplication of the augmented transformation matrix to generate the warp-correction of every focus-tunable lens plane to the reference. These matrices are calculated using the MultiStackReg plugin in Fiji (NIH). Since these deformations were due to the optical system, not motion of the sample, these corrections were applied to every volume prior to subsequent motion correction (Figure 5B, “Step 1”). For the Olympus microscope that uses a piezo microscope stage to scan axially, there is no deformation, and this step is skipped.

Due to rapid motion caused by mouse movement, it was necessary to account for intra-volume changes. Using the brightest plane as a stationary anchor plane, each plane was registered to its neighbor, using Fourier cross-correlation to estimate the X and Y shifts. These neighboring X and Y shifts were summed cumulatively so that each plane is aligned with the anchor plane. (Figure 5B, “Step 2”) (Guizar-Sicairos and Fienup, 2008).

After intra-volume alignment, reference volumes were generated by averaging every 20 volumes. To account for inter-volume lateral and axial shifts, each volume was then registered to its respective reference volume by cross-correlating the 3D Fourier transformation of the two volumes to find the X, Y, and Z shifts. Each reference volume was registered to the first reference volume using the same method (Figure 5B, “Step 3”).

Axial projections, such as mean, median, and maximum projections, were then performed (Figure 5B, “Step 4”). Finally, the movie of these projected images was further stabilized in three successive steps: (i.) matching each frame to the average of the first 50 frames, (ii.) matching each frame of the resulting movie iteratively to its neighbor, (iii.) matching each frame of the resulting movie to the average of the first 50 frames (Figure 5B, “Step 5”).

To estimate the degree of brain motion of ChP *in vivo*, we quantified the two kinds of correction for brain motion that were applied (see above). The first correction involved intra-volume XY displacements for each plane (Figure 5B, “Step 2”). The second involved inter-volume displacements from 3D translational registration (Figure 5B, “Step 3”), together with additional XY displacements common to all planes and derived from the registration of the 2D image stack resulting from axial mean projections of each volume (Figure 5B, “Step 5”). The intra-volume XY displacement reflected faster frame-to-frame motion within a given Z-scan (12.8–31 frames per second; 31–81 frames per volume). We quantified the distribution of intra-volume XY displacements using the Euclidean distance of intra-volume shifts in X and Y. We also calculated inter-volume displacements between successive volumes (0.16–0.97 volumes per second) to estimate the level of motion observed at these somewhat slower timescales (using the using the Euclidean distance of X and Y displacements between consecutive volumes, ΔXY, and using the absolute value of the shift in Z between consecutive volumes). These distributions were then expressed as cumulative distribution functions for each recording (Figures 5G and 5H). Overall, the degree of brain motion was substantially larger than what is observed for recordings in other brain regions such as in the neocortex.

Inter-volume motion artifacts

To assess the efficacy of our 3D registration in removing motion artifacts, we considered sets of five consecutive volumes of the red channel (vasculature), which was expected to be stable (i.e., near-constant voxel intensity) in the absence of brain motion at this

timescale. Thus, we used the metric of local standard deviation as a proxy for inter-volume motion artifacts. A rolling standard deviation across five neighboring volumes was calculated for each 3D voxel. These standard deviation contributions were averaged to obtain a global estimate of image stability. To account for global intensity changes within and across recordings, we normalized this mean standard deviation signal by the mean fluorescence to obtain an estimate of inter-volume motion artifacts over time.

Re-registration of single-cell regions

After 3D registration of the entire region, individual cell regions of interest (ROIs) were selected for local re-registration. XYZ regions were determined manually. The selected regions were then re-registered in XY with Fourier transformation-based cross-correlation, and individual plane affine registration, as described in the “3D registration” section, above.

Recording “physiological housekeeping” by immune cells

To assess the uptake of dextran by immune cells, a 3D recording of the ChP was acquired for 1 hour before the injection of 70 kDa red dextran. Immediately after this recording, without moving the recording field of view, the mouse was injected with 70 kDa red dextran, and recorded for 1 hour, as the dextran filled the vessels. Another 48 hours later, using local vascular features and tissue morphology, we imaged the same volume of ChP for an additional hour, without injecting more red dextran. All three recordings used the same acquisition parameters.

Response to LPS

To elicit a peripheral inflammatory response, 5 mg/kg lipopolysaccharide (LPS, Sigma) was delivered i.p. (Monje et al., 2003). An equal volume of saline was used as a control.

Quantifying *in vitro* “vessel coating” by immune cells

To quantify immune cell alignment with the periluminal region immediately adjacent to vessels, whole-mount LV ChP explants of LPS- and saline-injected $Cx_3cr_1^{+/GFP}$ mice were isolated and immunostained for GFP to label immune cells, and PECAM to label vasculature. Using a 500 pixel x 500 pixel ROI ($225 \times 225 \mu\text{m}^2$), the image pixel intensities were rescaled to the range 0-1 (20th percentile of pixel brightness rescaled to 0; 90th percentile of pixel brightness rescaled to 1). A first step to defining the periluminal region was to develop an automated algorithm to segment the vasculature. Segmenting vasculature involved identifying image regions that contain tube-like structures. Additionally, these tubes may be of different sizes (e.g., capillaries versus veins), and may also join together in junctions. Based on this structural description, a Jerman filter (Jerman et al., 2016) based on the local second-order derivative of the image (filter widths from 8 to 15 pixels; regularization factor $\tau = 1$) was used to enhance pixels that were part of tube-like structures. The resulting image was then binarized to separate vasculature from the background.

To validate the automated vessel segmentation algorithm used as an initial step toward defining periluminal space surrounding vessels, the vasculature image was manually segmented as a ground truth comparison. Using the Selection Brush tool in Fiji, the vessels were hand traced and converted to a manual binary mask. The same region was automatically segmented, as above, to generate an automatic binary mask. The automated and binary masks were compared with the contour matching function, `bfscore.m`, in MATLAB. Briefly, the Boundary F1 score measures the how closely a predicted boundary matches a ground truth boundary. This algorithm was chosen over Dice or Jaccard similarity coefficients, as our principal goal involved defining the accuracy of the estimate of periluminal boundary.

To obtain an estimate of periluminal space, the edge of the binary image of vasculature (see above) was then dilated with a disk kernel with a width of 5 pixels ($\sim 1.6 \mu\text{m}$). Pixels belonging to this dilated mask but not to the original vascular mask were considered to belong to the periluminal region.

Pixels containing immune cell bodies or processes were defined as follows, from the green emission image. First, the image pixel intensities were rescaled to the range 0-1 (10th percentile of pixel brightness rescaled to 0; 98th percentile of pixel brightness rescaled to 1). The image was then binarized, and dilated using a disk kernel with a width of 5 pixels. The degree of immune cell process occupancy within the periluminal region (“vessel coating”) was estimated as the proportion of vessel edge that overlapped with the binarized and dilated immune cells.

In vivo vessel coating

To quantify *in vivo* changes in immune cell occupancy of periluminal regions near vessels in response to LPS, a four-hour, four-dimensional (X Y x Z x T stack) dataset was mean-projected along the Z axis to produce an XYT image stack. This image stack was downsampled to 120 volumes (by averaging successive sets of 30 volumes), to improve the signal-to-noise ratio. This image stack was split into two channels: immune cells and vasculature. To define the periluminal region, vascular image stack intensity levels were rescaled to the range 0-1 (20th percentile of pixel brightness rescaled to 0; 98th percentile of pixel brightness rescaled to 1), and registered using the MultiStackReg function in Fiji, based on motion estimates from the immune cell image stack (NIH). A median projection of the vascular channel was computed, and pixels belonging to vessels were enhanced relative to the background using a Jerman filter (Jerman et al., 2016) (filter width from 8 to 10 pixels; regularization factor, $\tau = 1$; see above). The gradient of the Jerman filtered image was calculated to find the vessel edges, and the gradient image was binarized, and morphologically

closed (dilation, followed by erosion of a binary image, resulting in the filling of small holes; the structuring element was a disk with radius of 2 pixels), defining the periluminal regions of the image.

The immune cell image stack intensity levels were rescaled to the range 0-1 (10th percentile of pixel brightness levels, rescaled to 0; 98th percentile of pixel brightness levels, rescaled to 1). For each time frame in the image stack, t , the fluorescence in the periluminal region, $F(t)$ was calculated as mean pixel intensity in the periluminal region defined above.

GFP fluorescence in the periluminal region, $F(t)$, was measured at each frame in the image stack as the mean immune cell pixel intensity in the periluminal region defined above. The average fluorescence in the 1 hour prior to LPS injection was used as a baseline, F_0 . Change in fluorescence in response to LPS was expressed as: $\Delta F/F_0$.

Immune Cell Imaging During Acute Chp Injury

In this experiment, a local region of the ChP of an adult awake mouse was heated using the imaging laser, together with two-photon imaging of immune cells and vasculature prior to and following the heating. After one hour of imaging of 3D volumes of immune cells and vasculature (as detailed above) at 2x magnification and 30-40 mW power, the scan settings were changed to 8x magnification and ~150 mW for two minutes to induce focal heating of a local region of the tissue. Immediately following this tissue manipulation, the previous laser scanning settings were returned to observe immune cell activity in response to the focal damage.

Tracking immune cell acute response to laser burn injury

Immune cell body positions relative to the rectangular region targeted for focal laser heating were sampled every 5 minutes for 30 minutes before heating and in the one hour after heating. A distance transformation was used to calculate the closest distance from each cell to the rectangular injury site at each time point (using `bwdist.m` in MATLAB). Velocities of these cells toward the burn site ($\Delta \text{distance} / \Delta \text{time}$) were calculated for the 30-minute period before the injury, and separately for the 60-minute period after the injury. In cases where the cell entered the burn site prior to the end of the recording period, the velocity was calculated using the displacement that took place until the moment that the cell entered the burn site.

Other Supporting Experiments

Immunostaining and immunoblotting

ChP explants were dissected and fixed in 4% paraformaldehyde for 10 min at room temperature. Samples were incubated in primary antibodies overnight at 4°C and in secondary antibodies at room temperature for two hours. For ACTA2 staining, samples were permeabilized with 0.1% Triton X-100 in PBS prior to primary antibody incubation. For GFP and PECAM (CD31) staining, samples were blocked (0.3% Triton X-100, 5% goat serum in PBS) for 1 hour prior to primary antibody incubation. All samples were counterstained with Hoechst 33342 (Invitrogen, H3570, 1:10,000) and mounted onto slides using Fluoromount-G (SouthernBiotech). Standard protocols were used for immunoblotting.

Nearest-neighbor analysis

Locations of cell centers were selected using the Cell Counter plugin in Fiji. The tissue outline was drawn manually and made into a binary mask using Fiji. The nearest-neighbor distance was calculated for each individual cell, and the cumulative distribution function was plotted using the `spatstat` package in R (Badedy et al., 2015).

Simulated distributions based on a 2D Poisson distribution were generated iteratively 100 times. The mean of these simulated distributions yielded the “Poisson” estimate, while their extrema yielded a $p = 0.01$ acceptance interval.

Cytokine FACS array

Pure CSF samples were collected from the cisterna magna. Blood samples were collected by tail-nick one hour following saline or LPS injection. The samples were coagulated, centrifuged and diluted five-fold. Post-surgical CSF samples were diluted two- or three-fold; post-LPS CSF samples were not diluted. For the 13-plex cytokine FACS-ELISA analysis, all samples were processed according to the manufacturer’s instructions. After resuspension, the beads were run on a FACS Celesta (BD Biosciences) and FACS results were analyzed by LegendPlex v7.1 software.

Quantitative RT-qPCR

RNA samples were prepared using either the RecoverAll Total Nucleic Acid Isolation Kit (Ambion) or the mirVana miRNA isolation kit, following the manufacturer’s specifications. Extracted RNA was quantified spectrophotometrically and 100 ng was reverse-transcribed into cDNA using the ImProm-II Reverse Transcription System (Promega) or ABI High Capacity cDNA Reverse Transcription Kit (4368813, Thermo Fisher). Primers were purchased from Thermo Fisher (Taqman Gene expression assays, informed by “Best Coverage”) and q-PCR reactions were conducted performed in duplicate using Taqman Fast Univ. PCR Master Mix. Cycling was executed using the StepOnePlus Real-Time PCR System (Invitrogen) and analysis of relative gene expression was performed using the $2^{-\Delta\Delta CT}$ method (Livak and Schmittgen, 2001). Gene expression readouts were normalized to eukaryotic 18S rRNA or *Gapdh* as internal controls.

Transmission and Scanning EM

Lateral ventricle ChP tissue from adult mouse brain was micro-dissected and processed for EM using standard methods (Coulter et al., 2018).

QUANTIFICATION AND STATISTICAL ANALYSIS

To achieve robust and unbiased results while minimizing animal use, whenever possible, we focused on within-mouse comparisons (e.g., changes in immune cell motility before and after tissue injury, Figure 7I), which affords greater sensitivity. It was not possible for experimenter to be not blinded to experimental conditions, except in analysis of LPS versus saline control (Figure 7C). We attempted to adhere to principles of Good Laboratory Practice (<https://www.who.int/tdr/publications/documents/glp-handbook.pdf>). Unbiased results were obtained by prospectively defining exclusion criteria (e.g., acquisition criteria [alignment, image quality], viral expression/localization). All descriptions of statistical significance, statistical tests used, and exact values and representations of n can be found in the figure legends. Software packages used for statistical tests can be found in the STAR Methods Key Resource Table under Software and Algorithms.